UNIVERSITÁ DEGLI STUDI DI PADOVA

DIPARTIMENTO DI FISICA E ASTRONOMIA GALILEO GALILEI

Corso di Laurea Magistrale in Fisica

Towards an experimental investigation of current-induced forces on molecules deposited on graphene

RELATORE: Prof. Giovanni Mattei
CORRELATORE: Prof. Jan van Ruitenbeek

LAUREANDA: Irene Battisti

---

16 Settembre 2014

Contents

Chapter 1

Introduction

A steady flow of electrons through a conductor exerts a force on the atoms. In the presence of high current densities, this force can cause a displacement of the atoms: this phenomenon is called *electromigration*, and it is particularly enhanced at the micro and nanoscales.

Although a lot of experimental observations have been made regarding electromigration, either in bulk materials or on surfaces, a valid quantum mechanical description of this phenomenon is still lacking. The interpretation of electromigration experiments to date has been restricted to two standard phenomenological components of the driving force: the wind force and the direct force. The first one is caused by momentum transfer from electrons to atoms in each scattering event, and it acts in the direction of the electron flow. The second one is the force exerted by the electric field on the charged ions, and it can be in the opposite direction [1]. Recent experiments have begun to address the processes at the nanoscales, however the observations often have a difficult interpretation and do not always agree with the traditional theoretical description. There are some new theoretical developments presented in the work of Dundas et al. [2], in which it is shown, by analytical arguments, that the force exerted by an electron current on atoms is non-conservative. This interpretation could lead to new perspectives for the mechanism that drives electromigration, and moreover it could be the first step in the field of current-driven nanomachines that extract work from a current flow.

This thesis work consists of the preliminary studies of a project that aims to experimentally reveal and characterize the non-conservative force proposed by Dundas et al. [2].

The goal of the project is to study the current-induced motion of single molecules deposited on graphene, with the use of a UHV Scanning Tunneling Microscope. Studying current-induced forces at the single molecule (or single atom) level is required in order to relate the experiment to the theory and reveal the microscopic mechanism that drives electromigration. The effects of current-induced forces are enhanced in presence of high current densities, therefore it is important to have a high and well-confined current density in the sample: graphene is a suitable material for this purpose, because it can sustain very high current densities without being damaged.

Ideally the measurements should be done at low temperatures, in order to minimize the thermal motion and allow to isolate and study single molecules and single atoms. However, the UHV STM on which the experiments are performed operates at the room temperature. In the second step, the project will proceed to the low temperatures STM of the research group. This instrument is not yet provided with a coarse XY stage movement and with two contacts on the sample holder to allow the current flow. Therefore it is useful to make the preliminary studies on a different instrument, in order to investigate the feasibility of the project, although without the facility of low temperatures.

The preliminary studies carried out in this thesis can be divided into two main sections. The first one consists of the design and fabrication of graphene samples by means of microfabrication techniques, such as e-beam lithography, plasma etching and thin metal film deposition. This is followed by the sample characterization and the establishment of the cleaning procedure suitable for STM measurements. The second section consists of STM studies of molecules deposited on HOPG (Highly Oriented Pyrolitic Graphite) by evaporation inside the UHV chamber. The goal is to find molecules that interact with the surface in a way that single molecules or small clusters can be isolated at the room temperature. Deposition of molecules is studied on HOPG instead of graphene since the first studies are carried out in parallel with the first graphene samples fabrication, and HOPG provides a surface that is similar to the surface of the graphene.

In Chapter 2, the traditional interpretation of electromigration is explained in details, as well as the new theoretical developments that are aimed to be investigated in the main project. Theory of STM and properties of graphene are also presented. The explanation of the experimental equipment used during the project is given in Chapter 3. In Chapter 4, the procedures for samples fabrication, cleaning and characterization are described. Chapter 5 reports briefly the theory of interaction between molecules and surfaces and the theory of tunneling spectroscopy on molecules, followed by the results obtained from STM studies on molecules deposited on HOPG.

The project is carried out in Kamerlingh Onnes Laboratories at Leiden University (The Netherlands), in the group Atomic and Molecular Conductors.

Chapter 2

Theoretical background

2.1 Electromigration

In the free electron model of conductivity, the conduction electrons move in the metal unconstrained by the lattice of ions, except for scattering interactions due to phonon vibration and lattice defects. The scattering is the cause of electrical resistance and Joule heating. When an ion is placed out of its equilibrium position, i.e. a diffusing atom at the activated state, it possesses a very large scattering cross section. The scattering does not enhance the displacement of the ion and it has no net effect on its diffusion when the current density is low. However, scattering by currents of high densities, above 10^4 A/cm^2, enhances atomic displacement in the direction of the electron flow. Moreover, the lattice ions are directly subjected to the externally applied electric field. The accumulated effect of the atomic displacement in the direction of electron flow and the influence of the electric field are called *electromigration* [1]. Electromigration becomes significant at the micro and nanoscales, where it can be either destructive or a useful tool to exploit.

Observations and studies of electromigration in bulk materials started in the 1930s, and one of its first applications was purifying metals: when a bar of metal is subjected to large currents for extended periods of time, impurities are driven to one end of the bar.

The study of electromigration in metallic thin films was initiated at the beginning of the 1970s, after it was identified as the cause of cracks formation in aluminium conductor lines [3]. In bulk metals, the dissipation of Joule heating sets a limit on the maximum current density to 10^4 A/cm^2, before reaching the melting point of the material. For semiconductor integrated circuits, which are deposited on insulating substrates that have good heat conductivities, it is easy to reach current densities up to 10^6 A/cm^2 with the device operating at the room temperature, thus electromigration becomes a significant effect. Most of the early studies of electromigration in metallic films were therefore carried out in the industrial laboratories with the emphasis on the reliability problem of failures in semiconductor integrated circuits.

More recently, in the field of nanoscience and molecular electronics, controlled

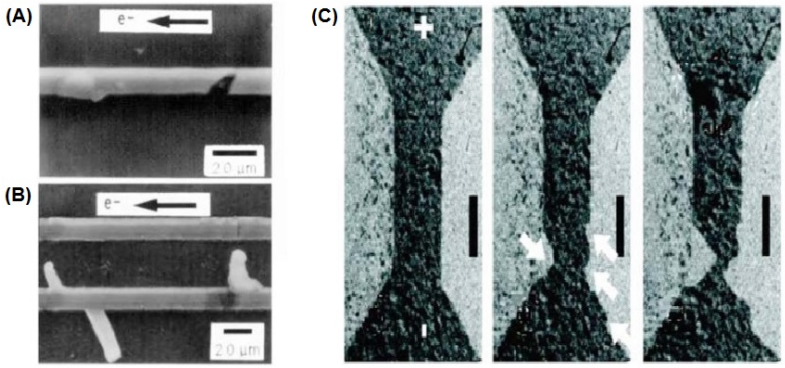

Figure 2.1: **(A)** , **(B)** SEM images of open circuit failures (formation of voids) and short circuit failures (formation of hillocks) caused by electromigration in a microfabricated circuit. **(C)** TEM images of the controlled breaking of a 12 nm thick Au nanowire at three successive stages of the breaking process. The bias is applied such that the top electrode is positive. By ramping up the current, voids form at the cathode side of the wire (arrows), while hillocks can be observed at the anode side. The nanowire then breaks by electromigration. The scale bars are 200nm. Adapted from [7].

electromigration has been exploited as a fabrication technique. Conductance of single molecules can be studied by placing the molecule between two electrodes that are a few nanometers apart. Electromigration, together with the mechanically-controllable break junction technique, provides a way to produce controlled and reproducible nanogaps: a current is passed through a narrow metal wire until it breaks and forms two closely spaced contacts (Fig. 2.1(C)). By depositing molecules of interest on top of the wire before electromigration, it is possible to make contact to single molecules [6].

2.1.1 Classical interpretation of electromigration

In the classical interpretation of electromigration the driving force consists of two components, the *direct force* and the *wind force* [1]. The direct force is the force that the electric field exerts on the ion. The wind force is caused by momentum transfer of the current carriers onto the atom during the scattering process. The electron wind force is usually dominant and it can be opposite in direction to the electrostatic force.

The first and simplest model of electromigration was developed by Fiks in 1959. It is a ballistic model, in which the driving force $\vec{F}$ acting on a single atom can be expressed by

$$\vec{F} = Z^* e \vec{E}$$

where e (> 0) is the elementary charge, $\vec{E}$ is the electric field, and Z^* is the effective charge number, given by

$$Z^* = Z_{el} + Z_w$$

The electrostatic part Z_{el} of the effective valence is related to the direct force. The wind part is given by

$$Z_w = -n\lambda\sigma$$

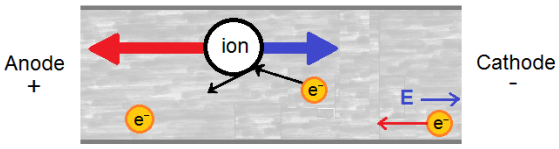

Figure 2.2: Classical model of electromigration: the wind force due to momentum transfer is in the direction of electron flow, while the direct force is the electrostatic interaction with the field.

where n is the numeric density of electrons, λ is their mean free path and σ is the scattering cross section of a mobile atom. Z_w can be easily derived as follows. The momentum transferred from an electron to a mobile atom in a single scattering event is

$$\Delta\vec{p} = -e\vec{E}\tau = -e\vec{E}\lambda/v$$

where τ is the collision time for electron scattering by atoms and v the average microscopic velocity of electrons. The wind force is the total momentum transferred to the mobile ion in a unit of time:

$$\vec{F} = -n\sigma v e\vec{E}\tau = -n\lambda\sigma e\vec{E}$$

from which the expression for Z_w can be easily derived. $n\lambda\sigma$ is the number of conduction electrons contained in a cylinder of lenght λ and cross section σ. Typically $\sigma \sim 1$ Å^2 and $\lambda \sim$100 Å, which gives cylinder volume of the order of 100 Å^3, much greater than the volume of a unit cell. Therefore in the cylinder volume there is a larger number of electrons in comparison to Z: this means that the effect of wind force is dominant compared to direct force.

After the simple ballistic model of electromigration, the first quantum mechanical description was proposed by Bosvieux and Friedel (1962) and later on refined by Sorbello (1975). Sorbello stated that it is possible to calculate the force exerted on the ion by the electron charge density in the presence of current, just as in the calculation of the force-field for a close system without current, on the basis of the Born-Oppenheimer adiabatic approximation (Appendix A).

Assuming that the atom of interest has valence Z and it is at the position $\vec{r}_0$, the bare potential seen by the electrons at $\vec{r}$ is

$$V_b = \frac{-Ze^2}{|\vec{r}_0 - \vec{r}|}$$

The net force exerted on the ion due to the electron wind force and the macroscopic electric field $\vec{E}_0$ can be calculated with the Hellman-Feynman formula:

$$\vec{F}(\vec{r}_0) = Ze\vec{E}_0 - \int \delta n(\vec{r}) \frac{\partial V_b}{\partial \vec{r}_0} d^3\vec{r}$$

where $\delta n(\vec{r})$ is the part of the local electron density that depends on the electron current.

The appropriate effective force for the resulting electromigration is the average of $\vec{F}(\vec{r}_0)$ over the jump path:

$$\vec{F}_{eff} = \frac{1}{|\vec{r}_A - \vec{r}_B|} \int_{\vec{r}_A}^{\vec{r}_B} \vec{F}(\vec{r}_0) \cdot d\vec{r}_0$$

where $\vec{r}_A$ and $\vec{r}_B$ are the initial and the final position of the ion. Applying the time-independent perturbation method and carrying out the calculations to the first order, the wind force can be reduced to a form identical to that one of the ballistic model [1].

After the pioneer works discussed above, many other theories have been developed, using both semiclassical and quantum approach, leading to more refined theoretical results that take into account many possible corrections to the first theories and also try to look at the phenomenon in different ways. Even if the classical interpretation of electromigration has established that the driving force can be separated into wind force and direct force (which can indeed be useful to explain the experimental observations of some types of defects moving in the current direction or in the opposite direction), whether this *a priori* separation is right remains an open question. A lot of discussions have been made about the real existence of the direct force and there are calculations which attempted to treat the driving force as a unique entity, however no real conclusion has been reached yet.

2.1.2 State-of-the-art experiments

Theoretical treatment of electromigration is mainly focused on the single-atom level, however the experimental studies to date have been limited to the concerted motion of many atoms. Recent experiments have begun to address the processes at the nanoscale, e.g. in studying the motion of islands of single atomic height on flat surfaces, or the motion of nanoparticles on carbon nanotubes. In this section, we show how far the experimental studies in this area have advanced, and we support the idea that it is possible to drive a sufficient amount of current through graphene in order to induce transport of molecules on its surface. We also emphasize that the interpretation of experimental data on electromigration at the nanoscale level is still not clear, as well as their correspondence to the theory.

Electromigration on surfaces

In the work of C. Tao et al.[8], the current-biased displacement of monoatomic islands containing a large number of silver (Ag) atoms upon silver surface is studied by Scanning Tunneling Microscopy. Electrical currents through the substrate provide momentum transfer to atoms of the island, yielding a response in the motion that depends on the atomic diffusion mechanism: surface diffusion is easiest for free atoms on terraces or along terrace edges, and island displacement is most likely to occur via atomic attachment to island edges or motion along them. Therefore the island motion involves a shift of the center of mass without the net simultaneous

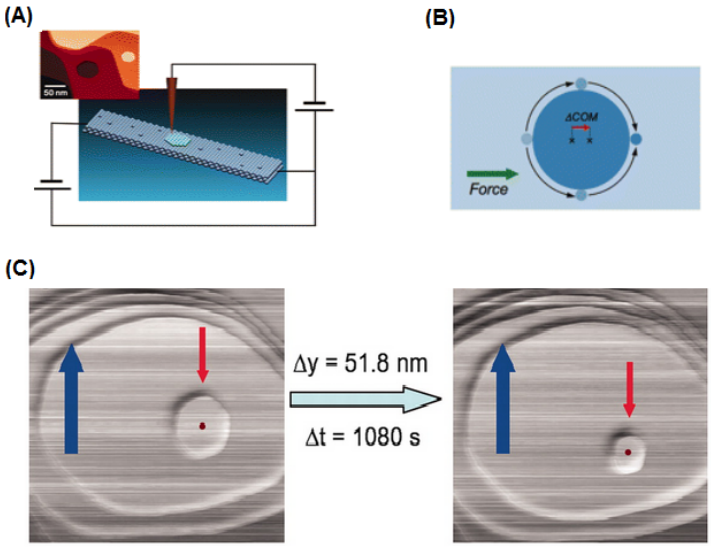

Figure 2.3: Electromigration induced motion of Ag islands on Ag surfaces. **(A)** Schematic drawing of the experiment. **(B)** Diffusion mechanism along island edges. **(C)** Biased displacement of a monolayer island driven by electromigration force. The current is in the direction of the blue arrows, while the electron flow is in the direction of the red arrow. The island moves in the direction of the electron flow. The shrinking is due to a thermal effect, and it is present even without the electrical current flow. The image size is 500×500 nm^2. Adapted by [8].

displacement of all the atoms in the island. They observe that the terrace displacement is in the direction of the electron flow and that the island drift velocity is inversely dependent on the island radius, from which they concluded that the main diffusion mechanism is motion along the island edges (Fig. 2.3B). The displacement (Fig. 2.3C) can be observed at a current density of $6.7 \cdot 10^5$ A/cm^2 and at a sample temperature of 318 K.

In the work of J. Moser et al.[13], the surface electromigration is exploited to clean graphene from contaminants due to lithographic steps. Graphene is able to carry very high electrical currents without sustaining damage, and, in this experiment, current densities up to 10^8 A/cm^2 are reached. The effects of these large current densities are electromigration as well as Joule heating. They study by Atomic Force Microscopy the motion of CdSe nanoparticles deposited on graphene, as well as PMMA (polymethyl methacrylate) residues of microfabrication process, and they find that the surface becomes smoother and cleaner after the current flow (see Fig. 2.4).

Electromigration on carbon nanotubes

In the work of K. Svensson et al.[10], it is shown that Fe nanoparticles can be transported by electromigration forces inside the hollow core of a multiwalled carbon nanotube. The nanotube is glued to the sample by one side and contacted by a piezo-driven STM tip on the other side. Using Transmission Electron Microscopy (TEM) they observe that, by driving current of sufficiently high densities, the iron inside the nanotube breaks into smaller particles, which then begin to move in the

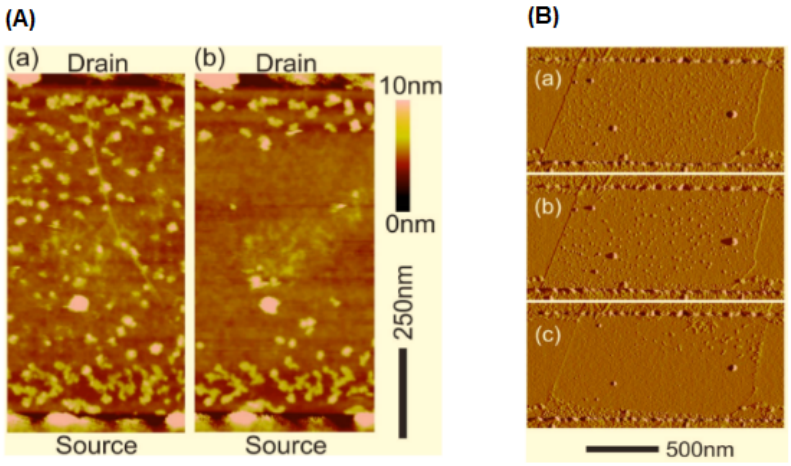

Figure 2.4: **(A)** AFM topographic maps of CdSe particles on graphene before (a) and after (b) applying a large electrical current between source and drain. **(B)** AFM signal amplitude scans captured at consecutive steps of the current-cleaning procedure. Adapted by [13].

direction of the electron flow (see Fig. 2.5). They measured the threshold current for iron diffusion in various nanotube sizes and they found that the threshold is in the current density rather than in the current, with a value around $7 \cdot 10^6$ A/cm^2. Together with the fact that by changing the sign of the current the motion of the Fe nanoparticles also changes direction, this provides a sufficient proof for the motion being induced by electromigration forces.

In the work of B. Regan et al.[11], they show that indium nanoparticles are transported on the surface of multiwalled carbon nanotubes when a current is driven through the nanotubes. In this experiment the nanotube is glued on the sample by one side and contacted by a tungsten tip on the other side. Using TEM they observe that, by driving a current through, mass is transported along the nanotube. The motion is inferred to be induced by electromigration forces since by inverting the current the direction of the nanoparticles motion is inverted. While in the experiment of Svensson [10] is observed that the movement of the iron particle is in the direction of the electron flow, Regan et al. [11] find that the direction of mass transport is against the current flow. Therefore in this case the direct force seems to prevail on the wind force.

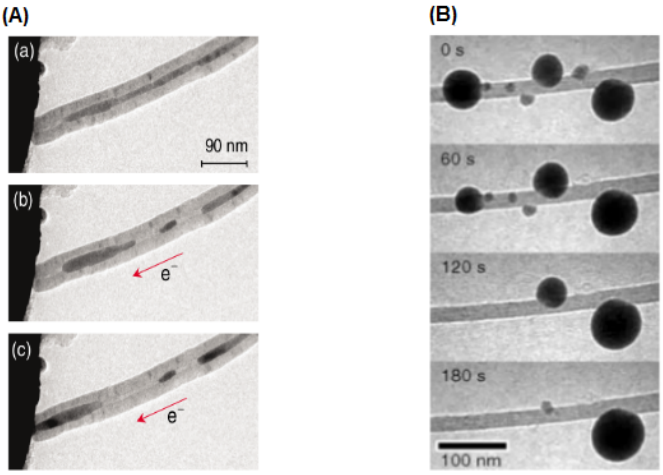

Figure 2.5: **(A)** TEM images showing the induced movement of iron nanoparticles: (a) the electrons flow from right to left at time t=0, (b) the iron core breaks up at t = 2 min, (c) iron particles migrate in the direction of the electron flow. Adapted from [10]. **(B)** TEM images showing transport of indium nanoparticles from left to right along single carbon nanotube. The electrons flow from right to left, therefore in this experiments the direct force seems to prevail on the wind force [11].

2.2 Non-conservative current-induced forces

The first suggestion about the possibility for the electromigration driving force to be non-conservative is made in a thought experiment by Sorbello [1]. He states that no assumptions are made about the force that drives electromigration being conservative: the work done by the force is not *a priori* assumed to be independent of the path taken between any two points. This is clear from the thought experiment where an atom is moved from one end of a long sample to the other, first by means of a path completely within the solid, and second by means of a path that is mostly outside of the sample. In the first case the wind force is always present, whereas in the second case there is no wind force.

The first calculations that take into account the possibility for the current-induced forces to be non-conservative are published by Dundas et al.[2]. They model a current-carrying atomic wire within the Ehrenfest approximation (Appendix A). To apply this method to steady-state conduction, they consider a nanostructure bonded to two semi-infinite electrodes with a bias voltage V applied across them (Fig 2.6). The steady-state electronic density matrix for the system, $\hat{\rho}(V, \vec{R})$, depends on the bias voltage and the atomic positions $\vec{R}$. The dependence on the atomic positions is due to the fact that atoms determine the potential to which the electrons are subjected. Therefore the steady-state electronic wavefunction and the density matrix are dependent on atomic positions.

By making use of Ehrenfest approximation, it is possible to calculate the forces that current-carrying electrons exert on atoms:

$$\vec{F}(V, \vec{R}) = \mathrm{Tr}\{\hat{\rho}(V, \vec{R})\hat{\vec{F}}(\vec{R})\} = -\mathrm{Tr}\left\{\hat{\rho}(V, \vec{R})\ \nabla\hat{H}\right\}$$

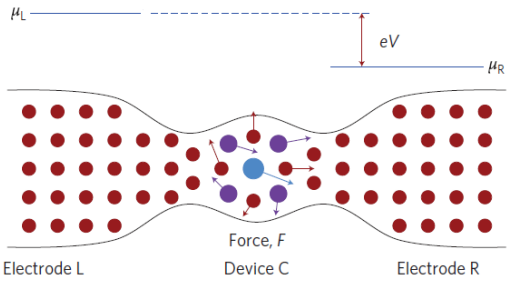

Figure 2.6: A generic device, in which dots of different colour represent atoms of different chemical identities, is bonded to two semi-infinite electrodes. The electrodes inject electrons with electrochemical potential $\mu_L = \mu + eV/2$ and $\mu_R = \mu - eV/2$, where μ is the Fermi level at equilibrium, $e(< 0)$ is the charge of the electrons and V is the applied voltage. Adapted from [2].

where $\hat{H}(\vec{R})$ is the electronic Hamiltonian, which depends on the classical ionic positions.

The steady state force thus obtained is a parametric function of the atomic position and the bias, and is free of any dissipative element, since electron-ion scattering is treated as purely elastic.

In order to show that the force exerted by the current is not conservative, they compute its curl, exploiting a formalism developed by Todorov [14]. To the lowest order in the bias, the curl calculation simplifies to

$$(\nabla \times \vec{F})_z = 4\pi \,\mathrm{Im}\,\mathrm{Tr}\{\hat{F}_x \hat{D}(\mu) \hat{F}_y \Delta\hat{\rho}\}$$

where $\hat{D}(\mu)$ is the density-of-states operator for the whole system and $\Delta\hat{\rho}$ is the non-equilibrium part of the density matrix, which is directly proportional to eV. Therefore the curl of the force vanishes at equilibrium, when the applied bias is zero. However, when there is a current in the system, the curl is non-zero: the force itself is not the gradient of a potential and it is not conservative. From a practical viewpoint, if the atom can be caught in a closed orbit, the non-conservative force can continually do work upon it, creating a nanoscale waterwheel.

In order to show that atoms can pick up energy from the electron flow, in the paper of Dundas [2] they investigate the dynamics of the corner atom of a bent atomic wire (Fig. 2.7(A)), by making use of nearest-neighbour single-orbital tight-binding model. The hopping integral is denoted by $H(< 0)$, and its derivative with distance is $H'(> 0)$. The corner atom is given an on-site energy E_c, while on-site energies of all the other atoms are set to zero. They calculate the current-induced force on the corner atom and they find that, if $|E_c| \ll |2H|$, the curl of this force is non-zero:

$$|\nabla \times \vec{F}| \approx |2eVH'^2 E_c/\pi H^3|$$

It is possible to estimate the amount of energy that the current-carrying electrons transfer to the atom, if we imagine the corner atom in a circular orbit of radius r. Thinking of the atom as a 2D oscillator of typical stiffness $K \approx 13\,eV\text{Å}^{-2}$, its energy is $U \approx Kr^2$ and the work done by the non-conservative force per revolution is $\Delta U_{nc} \approx |\nabla \times \vec{F}|\pi r^2$. For typical values as $E_c = 2\,eV$ and $V \approx 1V$, the fractional

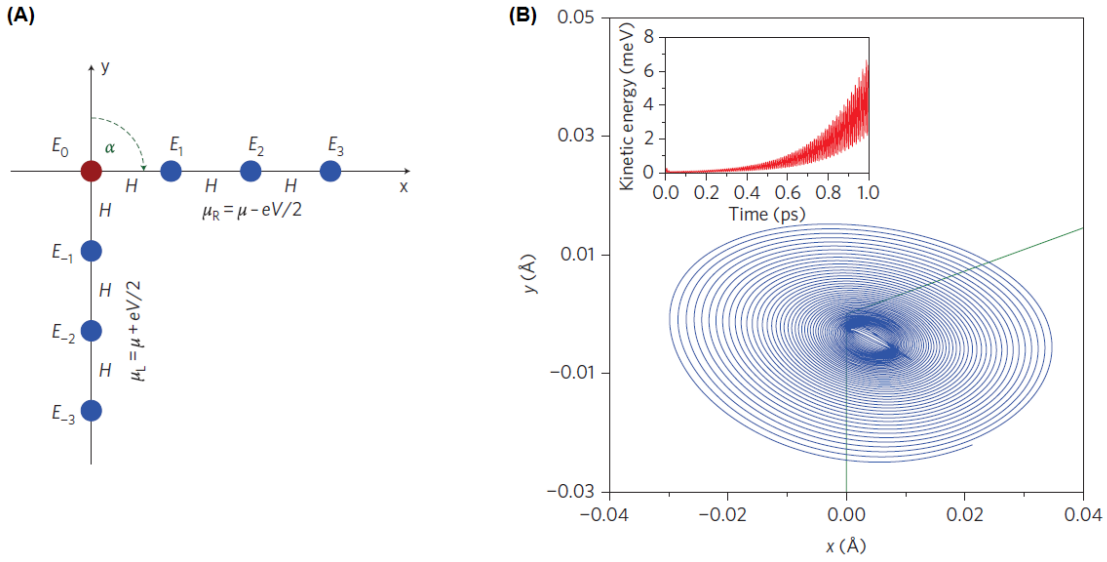

Figure 2.7: **(A)** Simplified atomic chain model used for the simulations of non-conservative current-induced forces. The red corner atom is affected by the current and it is allowed to move. **(B)** Periodic expanding orbit in the trajectory traced by the corner atom when the chain is bent by $\alpha = 70°$. The inset shows the increasing kinetic energy of the atom with passing of time. Adapted from [2].

increase in kinetic energy per period is then $\Delta U_{nc}/U \approx 1/5$, which is a sizeable effect.

An important factor which is ignored is inelastic scattering, which causes a damping effect. However the two effects, namely the non-conservative forces and the damping due to inelastic scattering, scale differently with the mass M of the ion, such that the non-conservative effect dominates for large masses, the ratio scaling as $\sqrt{M}$. The cross over between the two effects depends on the details of the atomic species and the type of bonding, however in general damping will be small except for the lightest element.

They test the calculation made for the corner atom of the atomic wire by means of dynamical simulations. By tuning the simulations parameters, in order to have a symmetric configuration in which the the two independent Einstein frequencies of the corner atom are equal, they show that the atom settles into an expanding orbit, nested within its initial position (Fig. 2.7(B)). This demonstrates the presence of the non-conservative force and its ability to drive a nanoscale waterwheel.

2.3 Scanning Tunneling Microscopy (STM)

Scanning Tunneling Microscopy was invented in 1981 by Gerd Binning and Heinrich Rohrer, who were awarded the Nobel Prize for the invention in 1986. The technique uses the concept of quantum tunneling to obtain real-space images of conducting surfaces: a sharp tip (in the ideal case monoatomic) scans the surface of the sample at a distance of a few angstroms, enabling electron tunneling between the tip and the surface, in order to measure the distribution of electronic surface states.

2.3.1 Operating principles of STM

A scheme of a typical STM is shown in Figure 2.8.

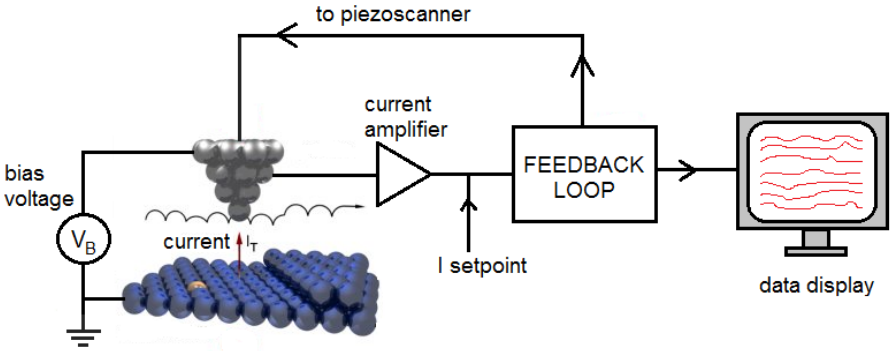

Figure 2.8: Scheme of the operating principles of STM.

The tip is moved back and forth across the sample surface by three mutually perpendicular piezoelectric transducers. Upon applying a voltage, a piezoelectric material expands or contracts: by applying a ramp voltage on the x piezo drive and a sawtooth voltage on the y piezo drive (or viceversa), the tip scans on the xy plane, filling the image line by line, while the z piezo drive probes the surface topography. When the tip and the sample are sufficiently close to each other, and a bias voltage is applied, a tunneling current occurs and it is amplified and converted into a voltage by a current amplifier.

The strenght of STM technique relies on the fact that the tunneling current has exponential dependence on distance between tip and sample, which allows to resolve atoms. There are two possible operating modes, constant current mode and constant height mode. In the *constant current mode* the tunneling current is set to a specific value (setpoint) and held constant by a feedback loop. The difference between the tunneling current and the setpoint value is amplified and used to drive the z-piezo motor: if the current is too high, the z piezo motor increases the distance between tip and sample, and vice versa. This leads to a tip height variation and thus the image comes from the tip topography across the sample and gives a constant charge density surface. In the *constant height mode* the distance between tip and sample is held constant and a different tunneling current is measured. Due to the exponential decay of tunneling current with distance, the constant height mode is

less precise, and even if it allows faster scanning speed, it can be used only on very flat surfaces. Hence the constant current mode is the most commonly used and all images presented in this thesis are obtained in this mode.

The topographic plot is displayed on a computer screen as a grey-scale image, since the information is given by the constrast: the bright spots represent high z values and the dark spots represent low z values. The height information detected by STM is always an apparent height, due to the convolution of the real height and the density of states of the tip and the sample.

Vibration isolation is essential to avoid crash of the tip on the sample while the tunneling distance is kept during measurements: the transmission of environment vibration to the STM unit is reduced by a vibration isolation system and by making the STM unit as rigid as possible.

The resolution of STM images depends on the shape of the tip: good atomic resolution is possible when there is a single atom on the apex of the tip, since the tunneling current mainly flows across the narrowest part of the barrier. With a blunt tip, where there is more than one atom on the tip apex, there are multiple channels for the tunneling current, therefore atomic resolution is not achievable.

The STM experiments can be performed in a variety of ambient conditions: in air, in inert gas, in ultra-high vacuum or even in liquids. The operating temperature ranges from absolute zero to a few hundred degrees Celsius.

2.3.2 Theory of tunneling in STM

An exact theoretical treatment of the tunneling process in STM is not possible since it requires a detailed description of sample and tip states: this is not obtainable for a low symmetry object like the tip, with mostly unknown shape and exact chemical composition. Moreover, the tip apex structure can even change during the measurement process.

In the following, we treat the elementary model of one dimensional tunneling, as well as the Bardeen model based on time-dependent perturbation theory, which is a more complete, however still simplified, description.

An elementary model

In order to understand the tunneling of electrons between the tip and the sample, we need to consider first the well known problem of tunneling through a one-dimensional potential barrier. The Schrödinger equation of the system is

$$-\frac{\hbar^2}{2m}\frac{d^2\psi}{dx^2} + V(x)\psi(x) = E\psi(x)$$

where the potential is given by a constant potential barrier:

$$V(x) = \begin{cases} 0 & \text{if } x < 0 \\ V_0 & \text{if } 0 \leq x \leq d \\ 0 & \text{if } x > d \end{cases}$$

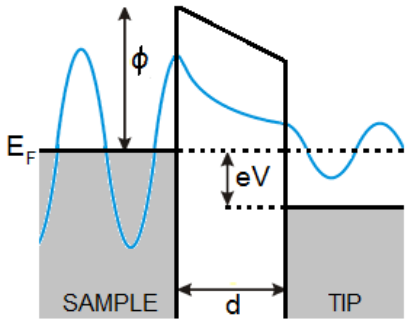

Figure 2.9: Tunneling process in STM. When the bias voltage is applied, electrons can tunnel from the sample to the tip.

The wavefunction $\psi(x)$ describing an electron with energy $E < V_0$ moving in the $+x$ direction in the classically forbidden region is

$$\psi(x) = \psi(0)e^{-\lambda x} \qquad \text{where} \qquad \lambda = \frac{\sqrt{2m(V_0 - E)}}{\hbar}$$

The probability P of observing an electron at the end of the potentail barrier ($x = d$) is $P \propto |\psi(d)|^2 = |\psi(0)|^2 e^{-2\lambda d}$.

When the model is used to describe the STM metal-vacuum-metal tunneling junction, the barrier height is provided by the work function[1] ϕ of the metal, and the barrier width is the distance d between the tip and the sample. To simplify the discussion we assume that the work functions of the tip and the sample are equal and we consider $T = 0$ K.

The electrons in the sample can thus tunnel into the tip and vice versa, however, without a bias voltage, there is no net tunneling current.

By applying a bias voltage V, a net tunneling current occurs (Fig. 2.9). An electron in the sample with eigenfunction ψ_n and energy E_n lying between E_F and $E_F - e \cdot V$ has the probability P to be present at the tip surface:

$$P \propto |\psi_n(d)|^2 = |\psi_n(0)|^2 e^{-2\frac{\sqrt{2m\phi}}{\hbar}d}$$

We assume that the bias is much smaller than the value of the work function, $e \cdot V \ll \phi$, so that the energy levels of all the sample states relevant for tunneling are very close to the Fermi level. The tunneling current is then proportional to the total number of states on the sample surface within the energy interval eV, leading to

$$I \propto \sum_{E_n = E_F - eV}^{E_F} |\psi_n(d)|^2$$

[1] The *work function* of a metal surface is defined as the minimum energy required to remove an electron from the bulk to the vacuum level. Neglecting the thermal excitation, the Fermi level is the highest occupied state in a metal, and taking the vacuum level as the reference point of energy, $E_F = -\phi$.

A useful concept is the *local density of states* LDOS, which gives the number of electrons per unit volume and energy at a given point and energy. The LDOS of the sample is defined at a location z and energy E, for a sufficiently small ϵ, as

$$\rho(z, E) \equiv \frac{1}{\epsilon} \sum_{E_n=E-\epsilon}^{E} |\psi_n(z)|^2$$

The tunneling current can be written in terms of the LDOS of the sample:

$$I \propto e \cdot V \cdot \rho(0, E_F) e^{-2\lambda d} \propto \rho(d, E_F) \cdot V$$

According to this analysis, a constant-current topographic STM image is a contour map of the sample surface (LDOS) taken at the Fermi energy and at the position of the tip. The exponential decay of the tunneling current with the distance d is found: the current decreases about one order of magnitude if d is increased by 1 Å, which is the reason that make STM such a powerful and precise instrument.

Bardeen's tunneling theory

Bardeen's tunneling theory was published in 1961 and applied to STM by Tersoff and Hamann in 1983. The prediction of this theory are considered trustworthy when the tip and the sample are sufficiently far apart and the bias voltage is low enough. Bardeen's approach is based on considering the tip and the sample as two separate subsystems and calculating the rate of electron transfer between the tip and the sample using time-dependent perturbation theory. This theory is based on several assumptions: tunneling is weak enough such that the first-order approximation of the time-dependent perturbation theory is valid; tip and sample states are nearly orthogonal; electron-electron interactions are negligible and therefore the single-electron Hamiltonian can be used.

The total separation of the tip and the sample leads to two independent Schrödinger equations:

$$(T + U_t)\psi^t = E^t\psi^t$$
$$(T + U_s)\psi^s = E^s\psi^s$$

where T is the kinetic energy operator, U_t and U_s are tip and sample potentials and the eigenfunctions ψ^s and ψ^t are called sample and tip states. The tunneling current is the result of the transfer of electrons from tip states to sample states (or vice versa) under the influence of the Hamiltonian for the whole system:

$$H = T + U_t + U_s$$

Considering the Hamiltonian of the whole system, a sample state ψ^s with energy E^s will evolve in time as:

$$\psi^s(t) = e^{-\frac{itE^s}{\hbar}} + \sum_k a_k(t)\psi_k^t$$

where the sum is over all the states of the tip Hamiltonian. Inserting the last equation into the time-dependent Schrödinger equation for the global system leads to:

$$i\hbar \sum_k \frac{da_k(t)}{dt}\psi_k^t = e^{-\frac{itE^s}{\hbar}} U_t \psi^s + \sum_k a_k(t)(E_k^t \psi_k^t + U_s \psi_k^t)$$

Taking the inner product with ψ_j^t and considering only the first approximation order results in the differential equation:

$$i\hbar \frac{da_j(t)}{dt} = e^{-\frac{itE^s}{\hbar}} \langle \psi_j^t | U_t | \psi^s \rangle + E_j^t a_j(t)$$

which can be solved for the initial condition $a_j(0) = 0$:

$$a_j(t) = \frac{e^{-\frac{itE^s}{\hbar}} - e^{-\frac{itE_j^t}{\hbar}}}{E^s - E_j^t} \langle \psi_j^t | U_t | \psi^s \rangle$$

Rewriting the matrix element $|M|^2 = \langle \psi_j^t | U_t | \psi^s \rangle$, the total transition probability is given by

$$P_{s\to t} = \sum_j |a_j(t)|^2 = \sum_j \frac{4sin^2[(E_j^t - E^s)\frac{t}{2\hbar}]}{(E_j^t - E^s)^2} |M|^2$$

If t is large enough, the sum can be approximated by the integral with respect to the energy, obtaining the Fermi's Golden Rule for the transition rate:

$$R_{s\to t} = \frac{d}{dt} \sum_j |a_j(t)|^2 \approx \frac{2\pi}{\hbar} |M|^2 \rho_{tip}(E^s)$$

where $\rho_{tip}(E^s)$ represents the density of states of the tip, which is the number of tip states per unit energy near to E^s. This would be the rate at which electrons in the sample state ψ^s are transferred into tip states of comparable energy, if all those states were vacant and available to receive electrons. However, due to Pauli's exclusion principle, the tip density of states needs to be multiplied by the fraction of unoccupied tip states:

$$R_{s\to t} = \frac{2\pi}{\hbar} |M|^2 \rho_{tip}(E^s)(1 - f_{FD}(E^s))$$

where f_{FD} is the Fermi-Dirac distribution:

$$f_{FD}(E) = \frac{1}{e^{\frac{E-E_F}{k_B T}} + 1}$$

In order to obtain the net current also the transition rate of electrons from the tip to the sample has to be considered, and it is multiplied by the fraction of occupied tip states:

$$R_{t\to s} = \frac{2\pi}{\hbar} |M|^2 \rho_{tip}(E^s) f_{FD}(E^s)$$

Assuming for simplicity tip and sample of the same material and applying a bias voltage V, the net current is given by the electronic charge e times the sum over sample states ψ_n^s of the difference between (i) the probability that the sample state ψ_n^s is vacant times the rate $R_{t\to s}$ and (ii) the probability that the sample state ψ_n^s is occupied times the rate $R_{s\to t}$:

$$I = \frac{2\pi e}{\hbar} \sum_{E_n^s = E_F - eV}^{E_F} \rho_{tip}(E_n^s)|M|^2[(1-f_{FD}(E_n^s))f_{FD}(E_n^s - eV) - f_{FD}(E_n^s)(1-f_{FD}(E_n^s - eV))]$$

In the case of $T = 0$ K the Fermi-Dirac distribution degenerates into the Heaviside step function, and the formula for the current becomes:

$$I = \frac{2\pi e}{\hbar} \sum_{E_n^s = E_F - eV}^{E_F} \rho_{tip}(E_n^s)|M|^2$$

As shown by Bardeen, the matrix element can be written in a symmetric expression as a flux integral through a generic separation surface in the barrier region:

$$M = -\frac{\hbar^2}{2m} \int_S (\psi_t^* \nabla \psi_s - \psi_t \nabla \psi_s^*) \cdot dS$$

Tersoff and Hamann applied Bardeen's formula to STM, approximating the tip to be spherical with radius of curvature R and modeling its electronic wavefunctions by radially symmetric wavefunctions:

$$\psi^t(\vec{r}) = A\frac{e^{-\kappa r}}{r} \qquad \kappa = \frac{\sqrt{2m\phi}}{\hbar}$$

The matrix element in this case becomes:

$$M \propto \kappa R e^{\kappa R} \psi^s(r_0)$$

where $\psi^s(r_0)$ is the sample wavefunction evaluated at the center of the tip. In the limit of small bias the final expression for the current is:

$$I \propto V \frac{R^2}{\kappa^4} e^{2\kappa R} \rho_t(E_F) \rho_s(E_F, r_0)$$

Therefore the tunneling current is proportional to the sample DOS ρ_s at the center of curvature of the tip. In this approach, the current can be related to a property of the surface alone and the interpretation of constant-current STM images is directly the contour of constant DOS at the Fermi level. However, a severe approximation is made on the structure of the tip and any tip dependence of the imaging is lost.

2.4 Graphene

2.4.1 Crystallographic properties

Graphene is a single two-dimensional layer of carbon atoms arranged in hexagonal structure. The structure can be seen as a hexagonal lattice with a two-atomic basis. Alternatively it can be described as two triangular sublattices, which have only one atom per unit cell, that are shifted by one atomic distance with respect to each other. The lattice vectors of the triangular sublattices are given by

$$\vec{a}_1 = \frac{a}{2}(3, \sqrt{3}), \qquad \vec{a}_2 = \frac{a}{2}(3, -\sqrt{3})$$

with the inter-atomic distance $a \approx 1.42$ Å. The corresponding unit cell is shown as shaded area in Fig. 2.10(A).

The reciprocal lattice of graphene resembles the hexagonal structure of the direct lattice. The reciprocal lattice vectors are given by

$$\vec{b}_1 = \frac{2\pi}{3a}(1, \sqrt{3}), \qquad \vec{b}_2 = \frac{2\pi}{3a}(1, -\sqrt{3})$$

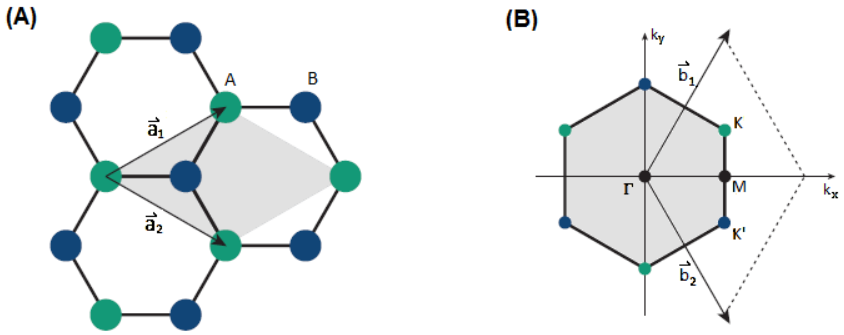

Figure 2.10: (A) Direct hexagonal lattice of graphene. Atoms of sublattices A and B are marked in different colors. The lattice vectors are given, together with the corresponding unit cell (shaded area). (B) Reciprocal lattice of graphene. High symmetry points K and K' are found at the corner of the first Brillouin zone (shaded area).

The resulting first Brillouin zone is shown in Fig. 2.10. High symmetry points Γ, M, K, K′ are denoted. The two points K, K′ at the corners of the Brillouin zone are not identical, since they correspond to two different atoms in the unit cell, and they are of particular importance for the physics of graphene. They are named Dirac points.

2.4.2 Electronic properties

All carbon atoms in graphene are sp^2 hybridized (one $2s$ orbital together with $2p_x$ and $2p_y$ orbitals generates three sp^2 orbitals), and each of these orbitals form σ-bonds with the orbitals of the neighbouring carbon atoms. These strong σ-bonds lie

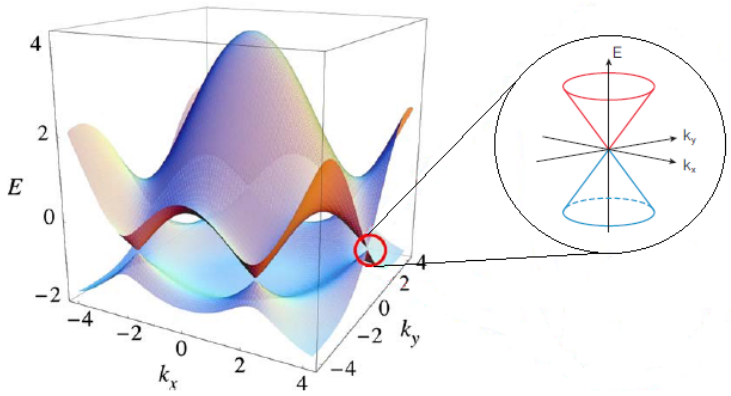

Figure 2.11: Band structure of graphene from tight-binding approximation up to the nearest-neighbour interaction. Valence band and conduction band touch in K and K′ Dirac points. An asymmetry between electrons and holes is visible. The insert shows the conical shape of the energy bands near to the Dirac points. Adapted from [19].

in-plane and are responsible for the honeycomb structure, as well as the mechanical stability of graphene. The σ-bands, however, play no role for charge transport in graphene, since they are separated by a sizeable energy gap.

There is one electron per carbon atom left in the $2p_z$ orbital, which is oriented perpendicular to the plane. The p-orbitals of different atoms overlap forming π-bands and π^*-bands of strongly delocalized electrons. These bands are responsible for most of the peculiar electronic properties of graphene.

From nearest-neighbour tight-binding calculations the structure of the π-bands can be derived [22]:

$$E^{\pm}(\vec{k}) = \frac{\varepsilon_{2p} \pm \gamma_0 \sqrt{f(\vec{k})}}{1 \pm s_0 \sqrt{f(\vec{k})}}$$

where $\vec{k}$ is the wave vector, and $f(\vec{k})$ is defined as:

$$f(\vec{k}) = 3 + 2\cos\vec{k}\cdot\vec{a}_1 + 2\cos\vec{k}\cdot\vec{a}_2 + +2\cos\vec{k}\cdot(\vec{a}_1 - \vec{a}_2)$$

The three parameters ε_{2p}, γ_0 and s_0 are found by fitting experimental or first-principles data.

Graphene is a zero-gap semiconductor, since the π^* conduction band and the π valence band meet at the Dirac points K and K′ (Fig. 2.11). The π energy-bands are cosine-like, therefore when they intersect at zero energy at the Dirac points, for low enough energy ($|E| < 1$eV [18]), the dispersion relation is approximately linear and the band structure acquires a conical shape.

In the literature, only the region around K and K′ is typically considered, since the Fermi level lies close to the point of band crossing in realistic graphene samples. Therefore, reduced wave vectors $\vec{q} = \vec{k} - \vec{K}$ and $\vec{q}' = \vec{k} - \vec{K}'$ are used to describe states in the vicinity of the K and K′ points, and the energy dispersion takes linear

form:

$$E_{\pm}(q) = \pm\hbar v_F q$$

where $q = |\vec{q}| = |\vec{q'}|$ and v_F is the Fermi velocity. Plus and minus signs refer to electron and hole states, respectively.

Due to its peculiar band structure, charge carriers in graphene possess unique properties. In condensed matter physics the electronic properties of materials are usually well-described by the Schrödinger equation. However, due to the linear structure of the dispersion relation close to the Dirac points, low-energy charge carriers in graphene mimic relativistic quasiparticles and are more easily described with the massless (2+1)-dimensional Dirac-Weyl equation [17]. These quasiparticles are called massless Dirac fermions and can be seen as electrons that have lost their rest mass.

Therefore the low-energy quasiparticles can be described by the Dirac Hamiltonian expanded around K:

$$H_K = \hbar v_F \begin{pmatrix} 0 & k_x - ik_y \\ k_x + ik_y & 0 \end{pmatrix} = \hbar v_F \, \boldsymbol{\sigma} \cdot \mathbf{k}$$

or around K′:

$$H_{K'} = H_K^T = \hbar v_F \begin{pmatrix} 0 & k_x + ik_y \\ k_x - ik_y & 0 \end{pmatrix} = \hbar v_F \, \boldsymbol{\sigma}^\star \cdot \mathbf{k}$$

where $\mathbf{k}$ is the quasiparticle momentum, $\boldsymbol{\sigma}$ is the 2D Pauli matrix, and the Fermi velocity, $v_F \approx 10^6$ m/s $\approx c/300$, plays the role of the speed of light.

Therefore charge carriers in graphene behave like relativistic particles with an effective speed of light given by the Fermi velocity.

2.4.3 Synthesis

After graphene was successfully isolated in 2004 by Geim and Novoselov using the Scotch tape method, there have been many different processes developed to produce graphene. One of the primary concerns in graphene syntesis is producing samples with high carrier mobility and low number of defects. To date, the best graphene quality is still obtained with the mechanical exfoliation method. However, this is a process limited to a small scale production and it provides graphene flakes which are rarely bigger than 20 μm in the lateral dimension. In the following, the mechanical exfoliation technique and two of the other main techniques for graphene synthesis are presented.

In our experiment, we make use of CVD-grown graphene as the first investigation of the feasibility of the project, and we investigate the possibility of making use of better-quality mechanical-exfoliated graphene.

Mechanical exfoliation

The exfoliation process consists of a few simple steps. It involves cleaving of HOPG (Highly Oriented Pyrolitic Graphite) with Scotch tape and subsequently folding

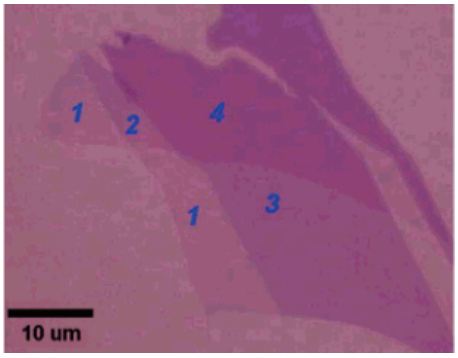

Figure 2.12: Mechanical exfoliated graphene deposited on SiO_2 under the optical microscope. Flakes of different thickness can be differentiated on the substrate. Numbers refer to number of graphene layer, determined by optical contrast and Raman spectroscopy. Adapted from [23].

over the Scotch tape several times upon itself. Once the tape is coated with a relatively thin layer of graphite, it is pressed onto a SiO_2-covered wafer. The result is a SiO_2 substrate with pieces from the graphite crystal and tape residue on top of it. The wafers can then be cleaned using chemical solvents.

The graphene flakes obtained in this way can be characterized under the optical microscope. Thin films of graphene are transparent, however, when deposited on a SiO_2-covered wafer, the added graphene layers generate light interference, causing a shift in colors that allows to distinguish the wafer from the graphene, and monolayer/few-layer graphene from multi-layer graphene (Fig. 2.12).

The few-layer graphene flakes produced by mechanical exfoliation are ballistic conductors at room temperature and have mobilities as high as 15000 $cm^2V^{-1}s^{-1}$ on Si/SiO_2 wafers [17].

Synthesis on SiC

The thermal decomposition of silicon carbide is a technique that consists of heating SiC in ultra-high vacuum to temperatures between 1000°C and 1500°C. This causes Si to sublimate from the material and leave behind a carbon-rich surface [24].

This technique is capable of making wafer-scale graphene layers [25]. Several issues still remain, such as a good control on the number of layers produced and interface effects with the SiC substrate.

Chemical Vapour Deposition

In chemical vapor deposition (CVD) of graphene, carbon is supplied in the form of methane and a metal is used, both as catalyst and as substrate to grow the graphene layer. The roughness of the substrate can lead to different corrugation of the graphene layer: growth on Cu(111) and Ni(111) is known to result in the most flat CVD-grown monolayers of graphene [26].

In order to use CVD graphene for nanoelectronic applications, it has to be transferred on an insulating substrate. Standard method consists of coating the graphene by a thin layer of polymethyl methacrylate (PMMA) and removing the

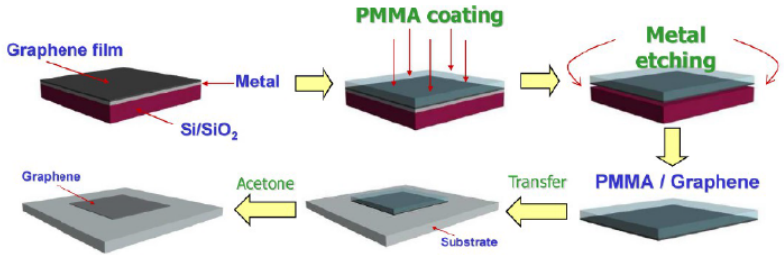

Figure 2.13: Scheme of the transfer process of CVD graphene to an insulating substrates [26].

metal layer by a dedicated etchant, leaving only PMMA/graphene film. The film is then cleaned by deionized water and then transferred onto the insulating substrate (typically a wafer of thermally grown SiO_2 on Si). After evaporating the water vapour away, PMMA is removed by acetone, leaving a graphene film on top of the substrate (Fig. 2.13).

Chapter 3

Experimental equipment

3.1 UHV Scanning Tunneling Microscope

STM measurements are performed using a commercial scanning tunneling microscope (JEOL). The setup has two chambers, the STM chamber and a sample treatment chamber, which are independently pumped down by means of ion pumps, ensuring operation under UHV conditions at a base pressure below 10^{-9} mbar.

The picture of the setup is presented in Fig. 3.1.

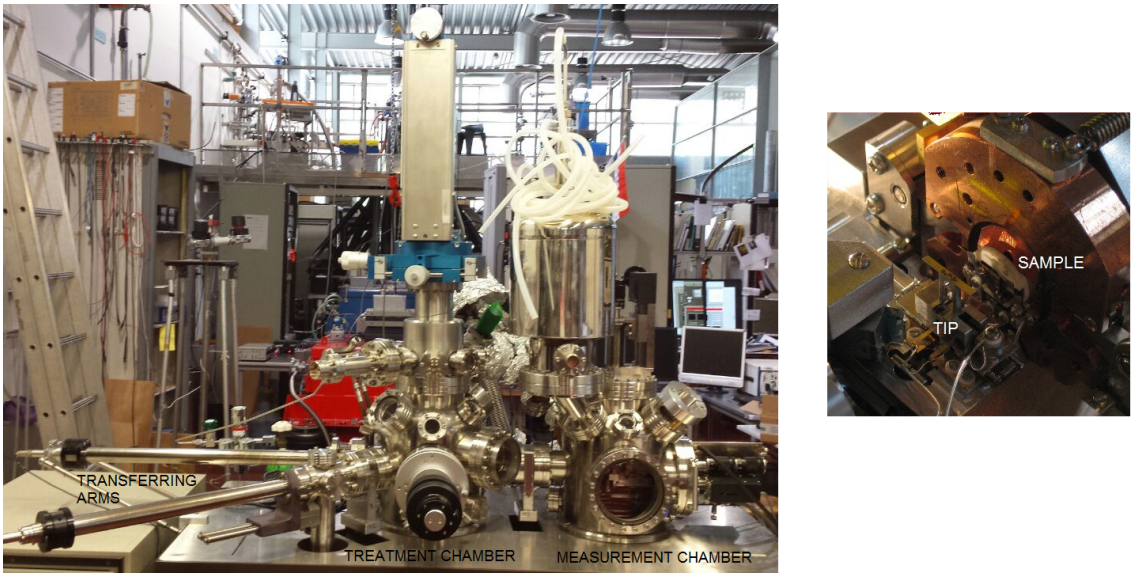

Figure 3.1: Picture of the STM setup used during the project and particular of the STM head, with tip and sample.

The sample and the tip are introduced via a separate load-lock chamber, where by means of a turbomolecular pump, the pressure of $\sim 10^{-6}$ mbar is reached. The sample can be transferred with the first magnetic arm in the treatment chamber, where it can be prepared for measurements: standard procedures are *in situ* temperature annealing by means of a button heater and evaporation of molecules on the surface by means of a Knudsen cell. With the second magnetic arm, the sample

can be transferred into the measurement chamber. Here the tip and the sample are brought to close distance first by a manual lever and then with an automatic approach controlled by the feedback system. During measurements the turbo pump of the load lock is switched off to avoid vibrations, while the ion pumps of the treatment and measurement chambers keep pumping.

The setup is provided with a Knudsen cell for evaporation, which is isolated from the treatment chamber by a gate valve, and has its own pumping system.

There is also the possibility to cool down the sample by means of a liquid nitrogen bath that is directly connected with the sample holder. However, when we tried to measure at low temperatures, we encountered a considerable thermal drift that prevented any measurement. A possible solution would be to make a better connection between the cold finger and the sample holder. However, in order to do that, the measurement chamber has to be opened. Since we did not have the certainty that it would have solved the problem, we chose to not use this facility during this project.

UHV

Solid surfaces are investigated in Ultra-High Vacuum (UHV) environment in order to minimize the interaction with foreign materials. The mean free path of molecules under a pressure of 10^{-9} mbar is about 10^5 m, therefore the molecules never meet each other, and they interact only with the chamber walls. The walls also host the majority of the molecules inside the chamber in the form of an adsorbate phase: if the surface of the chamber is heated, molecules desorb from it in enormous quantities. In order to achieve UHV conditions, a careful out-gassing has to be done by heating the system during the initial pump-down (bake-out), since the degassing process cannot take place once the pressure is already near the UHV range. Typical bake-out temperatures are 150-250°C. Construction materials must withstand these temperatures and must have a low enough vapour pressure. Classic construction metals for UHV are stainless steel for most parts of the vacuum chamber, copper for gaskets, and molybdenum and tantalum for parts to be heated to high temperatures.

Tip preparation

The performance of STM is much dependent on the condition of the tip, as it determines the resolution of the instrument. Ideally it has a monoatomic apex, however, while measuring, the tip continuously rearranges and sample atoms can adsorb during the operation. Since the image is a convolution of the tip and the sample, the symmetry of the tip is reflected in the recorded image. A blunt tip has difficulties to follow the smallest features of the surface, and a double-apex tip can cause the formation of artifacts on STM images.

Good tips can be prepared with a very simple method by taking a high quality conductor wire (usually Au or PtIr alloy) and cutting it to make it sharp. The trick to get good tips is to not cut the wire completely, but only indent it with the

cutter, while pulling on the wire. This will ensure that right before the cut occurs, the wire breaks instead: the action of breaking the wire in this manner creates a very sharp tip.
For the measurements reported in this thesis we use two different kind of wires for the tip:

- PtIr wire with diameter $\oslash = 250\,\mu$m;
- Pt wire with diameter $\oslash = 125\,\mu$m.

Knudsen cell

A Knudsen cell (K-cell) is used to evaporate organic molecules on the sample surface under UHV conditions. It exploits the principle of molecular effusion from a small aperture that gives rise to a cosine intensity distribution.

In our system the K-cell fits in an additional UHV chamber, which is mounted on the treatment chamber with a gate valve in-between. The K-cell chamber has its own pumping system (turbomolecular pump and ion pump), that can reach pressures of 10^{-8} mbar. The gate valve is opened only during the evaporation procedures.

Loading molecules in the K-cell implies opening the chamber and therefore breaking the vacuum. Each time molecules are loaded, the chamber needs to be pumped down from the atmospheric pressure and a 24-h bakeout has to be performed. During the bakeout procedures, the crucible with the molecules is kept at $\sim$20°C by the water cooling system.

The molecules to be deposited are loaded into the crucible, which is surrounded by a heating Tantalum foil. By applying a voltage, the source can be heated in a controllable way, in order to achieve a suitable vapour pressure in an isothermal enclosure. The reading of the temperature is provided by a thermocouple mounted at the end of the crucible. The furnace is surrounded by a water cooling system, in order to reach high temperatures only in the inner part of the K-cell, avoiding the heating of the chamber that can cause degassing of contaminants from the surfaces. The K-cell is provided with a shutter that is opened only during deposition, in order to have a good control of the deposition time.

3.2 Microfabrication

In order to have a sample where high current densities can be set up, we need to fabricate two metallic electrodes on a micrometric graphene surface. This can be done by microfabrication techniques, namely electron-beam lithography, plasma etching, metal film deposition and lift-off.

Electron Beam Lithography (EBL) is a fundamental technique for micro- and nanofabrication. The technique consists of using a beam of electrons to scan a surface covered with a resist film, in order to define the desired pattern on the resist. The resist is chemically changed under exposure to the electron beam, and the

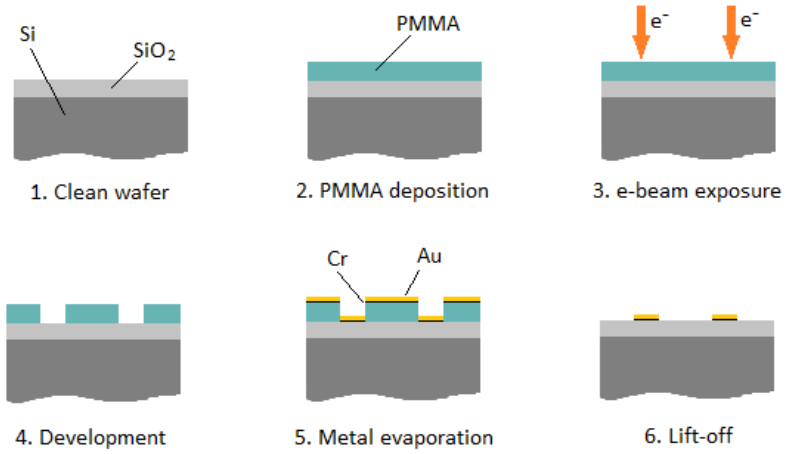

Figure 3.2: Scheme of a typical lithographic process.

exposed (or the non-exposed area, depending on the type of resist) can be dissolved in a specific solvent. The resist is called positive if the exposed area is dissolved in the solvent, while it is called negative if the non-exposed area is dissolved. In this project only positive resist is used, therefore in the following the processes are explained in the case of positive resist. After the removal of the exposed resist, a thin metallic layer is deposited on the substrate, followed by subsequent removal of the remaining unexposed resist (lift-off). The result is a sample with metallic structures only at places that were exposed with the electron beam (Fig. 3.2).

The main attributes of EBL are:

- its capability of very high resolution ($\sim$ 20 nm);
- its ability to work with a variety of materials and almost infinite number of patterns;
- its slow pace, being one or more orders of magnitude slower than optical lithography.

3.2.1 Spin coater and resist

To write structures using an electron beam, a layer of resist has to be put on top of the sample. A spin coater is used to deposit a uniform thin film, exploiting the centrifugal force. A drop of resist is put in the center of the substrate, which is then rotated at high speed in order to spread the coating material. After the spin coating process, a baking is performed using a hot plate.

The most commonly used e-beam resist (which is the one that is used during this project) is polymethyl methacrylate (PMMA). It comes in different molecular weights (50 - 950 kDa) and different dilutions.
According to the desired result, we use a single layer, as well as a double layer of resist with different weights and dilutions, and therefore different sensitivity to the

electron beam exposure (the lower the molecular weight, the higher the sensitivity to the electron beam):

- PMMA 200 kDa, solid contents 4% in Anisole (A4)
- PMMA 950 kDa, solid contents 4% in Anisole (A4)
- PMMA 950 kDa, solid contents 2% in Anisole (A2)

Spinning of the samples on the spin coater lasts for 5 sec at 500 rpm and for 60 sec at 4000 rpm. This results in a film thickness ∼250 nm for PMMA 200 kDa A4, ∼200 nm for PMMA 950 kDa A4, and ∼40 nm for PMMA 950 kDa A2 [29].

After the exposure with the e-beam, the resist is developed by making use of a diluted solution of MIBK:IPA 1:3. MIBK is the specific developer for PMMA, and it needs to be diluted with isopropanol (IPA) in order to give the correct development of the resist.

3.2.2 Electron-beam lithography

The e-beam lithography tool used for samples fabrication is a Raith e-Line 100 e-beam pattern generator (EBPG). It is composed of the following:

- a column, which contains an electron gun and magnetic lenses to focus and guide the beam;
- a specimen chamber, equipped with an XYZ-stage which is actuated in combination with a laser interferometer;
- a vacuum system which keeps column and specimen chamber in high vacuum ($< 2 \cdot 10^{-4}$ mbar);
- the operation and display system which analyses the signals and guides the electron optics.

Since the magnetic lenses can induce only a limited amount of deflection of the beam, the writefield area is limited. To be able to write large structures with high resolution, stitching of the different writefields is required, and it can be done using the movable XYZ-stage.

There are many parameters that can optimize the resolution of the writing process. The most important ones are the beam current, the area dose, the beam speed, and the area step size. These parameters are dependent on the beam spot size, the substrate and the type of resist. In order to find the best parameters, dose tests have to be done.

The minimum time to expose a given area for a given dose is provided by the following formula:

$$D \cdot A = T \cdot I$$

where T is the time to expose the object, I is the beam current, D is the dose and A is the exposed area. The user can set the desired beam spot-size, to which the current value is related. Small spotsizes correspond to small beam currents, and

thus long exposure times when large areas are to be exposed. Therefore, if large areas are to be exposed, it is better to use the biggest spot-size possible, which in our case is 700 nm.

Electron-solid interaction and proximity effect

Electron beam lithography tools are capable of forming extremely fine probes, however, when electrons hit the sample, scattering events broaden the beam and the resolution is reduced.

As electrons penetrate the resist, they experience many small angle scattering events (forward scattering), which tend to broaden the initial beam diameter. As the electrons penetrate through the resist into the substrate, they occasionally undergo backscattering events. In addition, the electrons are continuously slowing down, producing a cascade of low voltage electrons called secondary electrons.

The backscattered electrons may come back through the resist at a significant distance from the incident beam, causing additional resist exposure. This is called *proximity effect*: the dose delivered by the electron beam is not confined to the shapes that the tool writes, resulting in linewidth variations. For example, a narrow line between two large exposed areas may receive so many scattered electrons that it can develop away, while a small isolated feature may lose so much of its dose due to scattering that it develops incompletely. This effect is the reason for the resolution limit of ~ 20 nm.

3.2.3 Resistance evaporator

In order to deposit thin layers of metal on top of the sample after the e-beam exposure and development, a resistance evaporator is used. In this system the metal to be evaporated is heated up by driving a large current through a tungsten boat with the metal on top of it. The sample is placed in front of the evaporating metal, and the thickness of the deposited layer is measured by a crystal resonator which is placed near the sample.

The system operates in high vacuum, the main chamber is kept at a base pressure $P < 5 \cdot 10^{-8}$ mbar, and the samples are introduced using a loadlock.

The metal used to fabricate structures and contacts is gold. Due to a poor adhesion of gold to the substrate, a chromium layer is first deposited on the substrate, followed by gold deposition.

3.2.4 Plasma etcher

Oxygen plasma etching is used both for patterning the graphene, i.e. removing the graphene from undesired areas, and for cleaning the SiO_2 substrates from organic residues.

An Oxford PlasmaLab 90+ machine is used for this purpose. The system consists of a vacuum chamber with base pressure $P < 2 \cdot 10^{-5}$ mbar, which has a loadlock for loading the samples. Oxygen is introduced in the vacuum chamber and

O_2 plasma is created. The oxygen pressure, the oxygen flow, the power and the exposure time can be set manually.

3.2.5 Probe station

In order to check the contact on the microfabricated samples, a probe station is used. It consists of a table with microprobes placed inside a Faraday cage. The probes can be put on the contact pads with $\sim 50\mu$m precision with the use of an optical microscope. IV curves of the contacted graphene flakes can be recorded with the use of a LabView program, and the resistance of the samples can be measured.

Chapter 4

Sample fabrication and characterization

4.1 Requirements

The final purpose of the project is to observe by STM how molecules deposited on graphene move when a current passes through the graphene. In order to achieve this, we need samples with two separate metallic contacts on the graphene surface. The samples are then mounted on the STM sample holder. When the sample holder is in the STM measurement position, it is in contact with two clamps, between which a voltage can be externally applied.
The graphene with the two metallic contacts lies on an insulating substrate, and its surface is small enough to carry large current densities.
A schematic of the experiment is shown in Fig. 4.1.

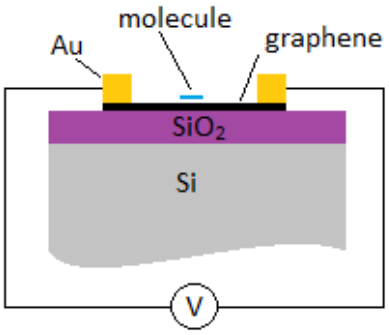

Figure 4.1: Scheme of the experiment.

We investigate two different graphene sources. The first one is CVD single/double-layer graphene provided by Graphene Supermarket [30]. It is grown on Cu(111) and transferred on 10×10 mm^2 Si wafers with a 285 nm layer of thermally grown SiO_2 on top. The second one is graphene mechanically exfoliated with Scotch tape method and transferred onto Si wafers with a 300 nm layer of thermally grown SiO_2 on top.

4.2 Preliminary investigation

Before the microfabrication processes, one of the graphene samples from Graphene Supermarket is observed and characterized by optical microscope and STM.

Optical microscope observation shows grain boundaries from the copper on which the graphene was grown, as well as some clusters of residues from the transfer process. The graphene fully covers the substrates and does not have significant cracks or holes (Fig. 4.2(A)). STM images in UHV conditions show typical structure of graphene deposited onto SiO_2 [32]: the graphene layer has a long-range corrugation, which is due to the structure of SiO_2 and to the possible presence of bubbles between graphene and SiO_2. A lattice structure is observable on the surface, however the interatomic distance is not comparable to the theoretical value (we find a$\sim$0.5 Å, and the theoretical value for graphene is a=0.14 Å). This could be due to a tip effect, as well as to the presence of a double layer of graphene, where the two layers are shifted with respect to each other, leading to a Moiré superstructure.

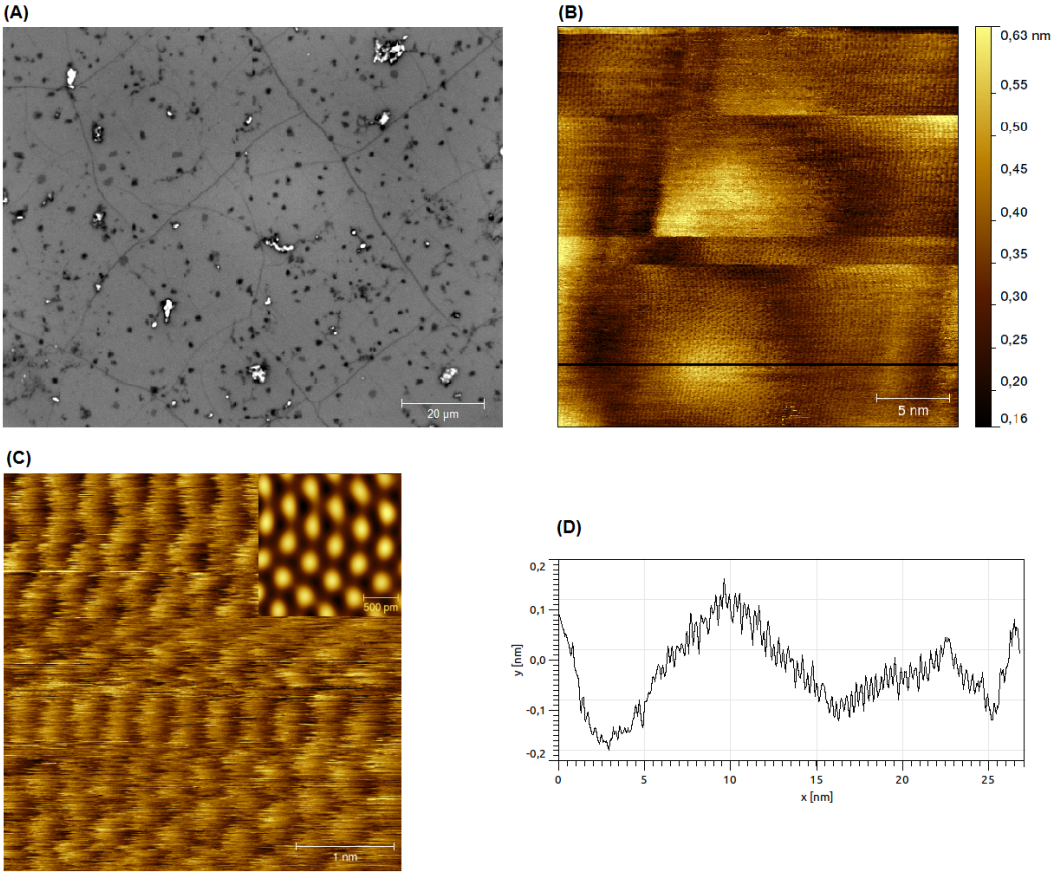

Figure 4.2: **(A)** Optical image of a graphene sample from Graphene Supermarket. **(B)** STM image (0.6 V, 1 nA) of the same sample. Atomic resolution is observed superimposed with a long range corrugation due to the substrate. **(C)** Zoom in on the image (B), (0.6 V, 1 nA). The inset shows a part of the filtered image obtained by selecting symmetry points in the 2D Fourier transform, enhancing the presence of an interatomic distance which is bigger then expected. **(D)** Line scan obtained along the black line in image (B).

4.3 Sample fabrication

4.3.1 Methods

In this section, the methods to obtain contacted graphene samples from Graphene Supermarket samples are presented.

The STM sample holder can host a wafer of maximum size 3.5×10 mm^2, therefore the wafers from Graphene Supermarket need to be cut in smaller pieces. The cleanest way to do so is to use a diamond cutter.
There are three fabrication steps to be executed: deposition of metallic alignment marks, etching of the graphene from the undesired areas, and deposition of metallic contacts on graphene. The presence of metallic alignment marks is required in order to write the contacts with the e-beam exactly on top of the patterned area of graphene.

An overview of the fabrication procedures is listed below, followed by the discussion of some important details.

Cutting wafers

1. We deposit a bilayer of PMMA 200k A4 ($\sim$ 250 nm) and PMMA 950k A2 ($\sim$ 40 nm) on the substrate. Each deposition is followed by 90 sec of baking on the hot plate at 180°C.
2. We make a small scratch on the front side of the wafer with a diamond cutter and break the wafer.
3. We rinse the substrate with DI water and dry it with N_2 flow.

Writing the alignment marks

1. We write 4 marks at the corners of the sample with the e-beam pattern generator (EBPG) using the following writing parameters:
   - spot size: 130 nm (PC 8, current I=0.4161 nA)
   - area dose: 300 μC/cm^2
   - total writing time: $\sim$ 60 sec.
2. We develop the resist by dipping the substrate in MIBK:IPA 1:3 for 40 sec.
3. We dip the substrate in IPA for 40 sec to stop the development.
4. We rinse the substrate with fresh IPA and dry it with N_2 flow.

Deposition of the metal

1. We deposit a 5 nm layer of chromium and a 25 nm layer of gold by evaporation.

Lift-off

1. We dip the substrate in acetone for at least 90 min at the room temperature.
2. We rinse with fresh acetone.
3. We rinse with IPA and dry the substrate with N_2 flow.

Patterning of the graphene

1. We deposit a layer of PMMA 950k A4 ($\sim$ 200 nm) and bake on the hot plate at 180°C.
2. We write the graphene etching mask exposing with the e-beam the area where graphene has to be removed, with the following writing parameters:

   - spot size: 700 nm (PC 1, current I=11.291 nA)
   - area dose: 250 μC/cm^2
   - total writing time: $\sim$ 30 min.

3. We develop the resist by dipping the substrate in MIBK:IPA 1:3 for 40 sec.
4. We dip the substrate in IPA for 40s to stop the development.
5. We rinse the substrate with fresh IPA and dry it with N_2 flow.

Etching of the graphene

1. We etch with oxygen plasma for 30 sec with the following parameters:

   - Pressure: 30 mTorr
   - Oxygen flow: 30 sccm
   - Power: 30 W

2. We put the substrate in acetone at the room temperature for 15 minutes in order to remove the remaining PMMA from the sample.

Writing the contacts

1. We deposit a bilayer of PMMA 200k A4 ($\sim$ 250 nm) and PMMA 950k A2 ($\sim$ 40 nm) on the substrate and bake for 90 sec on the hot plate at 180°C after each deposition.
2. We write 2 contacts on graphene with the e-beam pattern generator (EBPG) using the following writing parameters:

   - spot size: 700 nm (PC 1, current I=10.441 nA)
   - area dose: 250 μC/cm^2
   - total writing time: $\sim$ 25 min

3. We develop the resist by dipping the substrate in MIBK:IPA 1:3 for 40 sec.
4. We dip the substrate in IPA for 40s to stop the development.
5. We rinse the substrate with fresh IPA and dry it with N_2 flow.

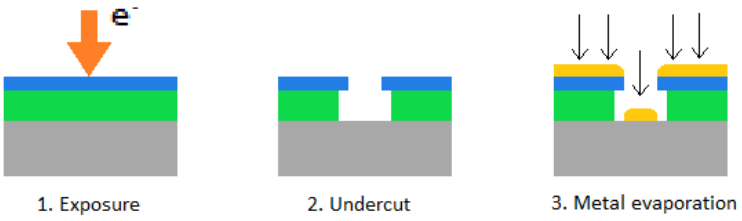

Figure 4.3: Advantage of using a bilayer of resist during metal deposition: the undercut, together with metal evaporation, results in a better quality lift-off.

Deposition of the metal

1. We deposit a 5 nm layer of chromium and a 50 nm layer of gold by evaporation.

Lift-off

1. We dip the substrate in acetone for at least 90 min at the room temperature.
2. We rinse with fresh acetone.
3. We rinse with IPA and dry the substrate with N_2 flow.

Monolayer vs. bilayer of resist: The use of a monolayer of resist (PMMA 950k A4) during the metal evaporation steps results in a difficult and bad-quality lift-off, in which large areas of unexposed resist do not lift off.
In order to obtain a better lift-off after the metal deposition, a bilayer of PMMA 200k A4/PMMA 950k A2 is used. The use of a more sensitive resist (with lower molecular weight) underneath a less sensitive one causes an undercut during the development, which results in a lift-off of better quality. This is due to the fact that metal deposition using evaporation by resistive heating results in a straight movement of the metal particles: the upper layer of resist acts as a mask for the metal beam and no metal is deposited on the sides of the pattern connecting the lower layers to the layers on top of the resist. (Fig. 4.3).

Positive vs. negative resist: We use a monolayer of PMMA 950k A4 for the oxygen plasma etching of the graphene. We want to etch the graphene away everywhere on the substrate except on a surface of $300\times300\mu m^2$, therefore it would save time to use a negative resist, where the not-exposed features are developed away. However, negative resists are known to leave more residues on the surface after the lift-off and are more complicated to treat. Therefore we use a positive resist and expose with the e-beam a larger area around the whole structure (Fig. 4.4).
An alternative approach would be to fabricate alignment marks and contacts in a first step and to etch the graphene structure in a second one. This approach would have the advantage of saving one lithography and evaporation step, and would make the sample fabrication faster. However, the adhesion of the contacts to graphene is much weaker than to SiO_2, and hence the risk of scratching away the contacts with the clamps of the STM sample holder is higher.

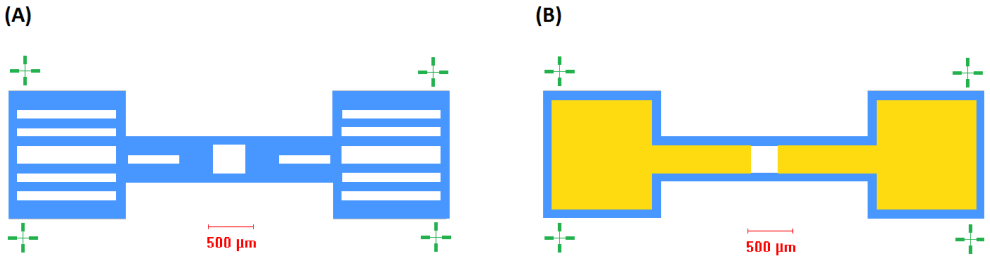

Figure 4.4: Schematic design (alignment marks are not in scale) of the processing steps that are necessary to pattern the graphene. After the deposition of the alignment marks (green), the PMMA mask for oxygen plasma etching is patterned (A): graphene is removed from the exposed areas (blue). Stripes in the contact area increase adhesion of the metal pads to the substrate. The last step is deposition of the contacts (B). In the final result, the white substrate area is graphene, the blue one is SiO_2 where the graphene is etched away, and the yellow one are the Cr/Au contacts.

Writing parameters: Since we deal with relatively big structures, the writing parameters are not that crucial for the quality of the markers and the text. A dose test is performed to estimate the best exposure dose. An area dose of 300 $\mu C/cm^2$ produces the best quality for the markers. For the contacts, a smaller dose is required: an area dose of 250 $\mu C/cm^2$ results in a good quality of the structures.

Alignment: In the writing procedure we have to deal with three different coordinate systems: one for the stage, one for the design on the wafer, and one for the beam. For overlay purpose, both stage and beam have to be aligned to the design on the wafer, and this is done using the alignment marks. In order to reach micrometer accuracy, three of the marks are used to optimize the beam alignment: they are scanned by the software automatically and feedback is performed to optimize the beam deflection.

4.3.2 Mechanically exfoliated graphene samples

In parallel with the fabrication of the CVD graphene samples from Graphene Supermarket, we investigate another possible source of graphene. We started a collaboration with the research group of Dr. Gregory Schneider from Leiden Institute of Chemistry: they work on graphene and they provided us with some flakes of graphene deposited on SiO_2.

In order to be able to easily find and contact the graphene flakes after the deposition, we prepared an array of marks and numbers with lithography, followed by Cr/Au deposition, on a Si wafer with a 300 nm layer of SiO_2 on top. The array has a surface area of 1 cm^2, and it consists of a grid with 10 μm-sized crosses placed at a mutual distance of 100 μm. An additional grid is added in order to make easier to locate the flakes: every millimeter, the X and Y millimeter coordinates are written in large size.
The procedures used for writing the mark array are the same as presented before,

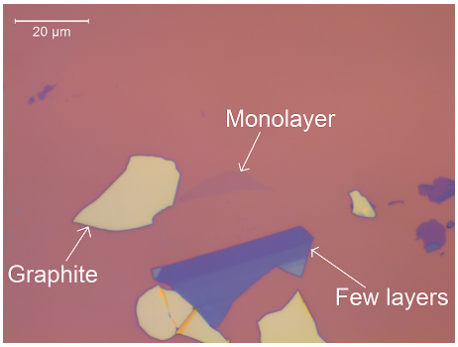

Figure 4.5: Mechanical exfoliated graphene deposited on SiO_2, under the optical microscope (M=100x). Flakes of different thickness can be differentiate from the substrate. A monolayer flake (light purple) is visible in the centre of the image. Few layers (intense purple/blue) and multilayers (yellow) are present in higher number and bigger lateral dimension.

with the following parameters:

- Marks
  - spot size: 130 nm (PC 8, current I= 0.0797 nA)
  - area dose: 300 μC/cm^2
  - total writing time: $\sim$ 4 h
- Numbers
  - spot size: 320 nm (PC 4, current I= 0.5620 nA)
  - area dose: 250 μC/cm^2
  - total writing time: $\sim$ 30 min

In order to clean the substrates from organic contaminants that could decrease the quality of graphene deposition, an oxygen plasma cleaning procedure is executed with the following parameters:

- Pressure: 30 mTorr
- Oxygen flow: 30 sccm
- Power: 50 W
- Time: 1 min

Graphene deposition with Scotch tape method produced only a few monolayer flakes, which are up to 20 μm-wide. Additionally, several few-layers flakes were produced, however none of them is bigger than 50 μm in the lateral dimension (see Fig. 4.5). These flakes are too small to secure a successful approach of the STM tip on top of it, therefore we do not make use of these samples.

4.4 Characterization of samples

Before mounting the samples on the STM sample holder, their conductance is tested in a probe station. The probe station is provided with 4 needles and it can perform 2-probe and 4-probe measurements.

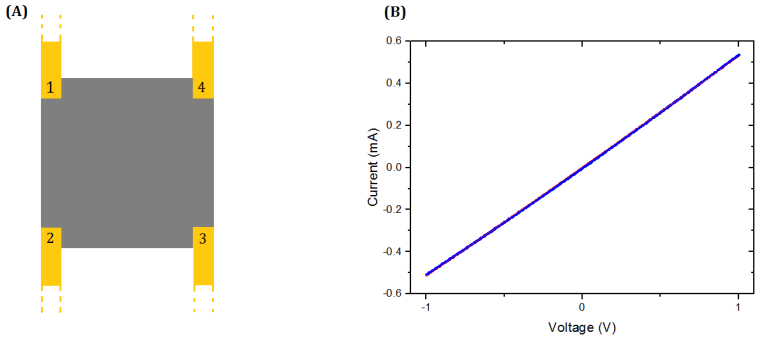

Figure 4.6: **(A)** Van der Pauw configuration for sheet resistance measurements. **(B)** Typical linear behaviour in the I-V curve of sample #3 in the 2-probe measurement. The resistance extracted from the linear fit of the data is R = (1.97 ± 0.01) kΩ.

The 2-probe configuration is used to directly measure the resistance of the samples. The needles are put on the two gold electrodes, a ramp voltage is applied, and corresponding current is measured by making use of a LabView program. The resistance of the sample can then be extracted from the linear fit of the data.

Device	Resistance 2 probes (kΩ)	Sheet resistance (kΩ/sq)
2 contacts #1	2.56 ± 0.03	-
2 contacts #2	2.84 ± 0.03	-
2 contacts #3	1.97 ± 0.01	-
4 contacts	2.96 ± 0.03	2.72 ± 0.01

Table 4.1: Resistance and sheet resistance measurements of 4 different graphene devices. The first three samples have only 2 contacts on the graphene, while the last one is provided with four contacts in order to perform a Van der Pauw measurement.

The 4-probe configuration is used to make a measurement of the sheet resistance of graphene in Van der Pauw configuration. The 4-probe measurement has the advantage of eliminating the contact resistance from the probes.
In order to make this measurement, a graphene area equal to the one fabricated in the samples is contacted at the 4 corners by 4 metallic pads (Fig. 4.6(A)). Two different measurements have to be executed to find the sheet resistance. First a current is applied between terminal 1 and 2, and the voltage drop is measured between terminal 3 and 4 with a digital multimeter. Resistance R_A is extracted. Then a current is applied between terminal 2 and 3, and the voltage drop is measured between terminal 1 and 4. Resistance R_B is extracted. The formula that connects these measurements to the sheet resistance R_S is a transcendental equation:

$$e^{-\frac{\pi R_A}{R_S}} + e^{-\frac{\pi R_B}{R_S}} = 1$$

If R_A and R_B are not too different, this formula can be solved by approximation:

$$R_S = \frac{\pi}{\ln 2}\left(\frac{R_A + R_B}{2}\right)$$

Since the shape of the graphene samples is a square, the sheet resistance corresponds to the actual resistance.
The resistance values obtained from 4 different devices and the sheet resistance are listed in Table 4.1. The values extracted from the 2-probe measurement and the 4-probe measurement are not significantly different, therefore the contact resistance does not play an important role in our devices.

4.5 Samples in the STM setup

After the characterization of the sample conductivity at the probe station, the sample is mounted on the STM sample holder by means of two clamps which make electrical contacts with the gold contacts from microfabrication.
The sample holder is transferred in the STM measurement chamber, where, with the help of an optical microscope and use of the coarse stage movements, the tip is brought in front of the graphene surface (Fig. 4.7).

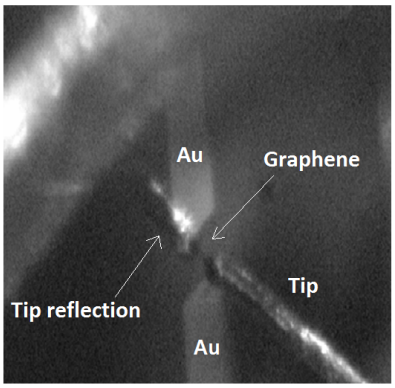

Figure 4.7: Optical microscope image of the tip and the sample inside the STM setup. The reflection of the tip on the sample is clearly visible. The size of the graphene is $300 \times 300\,\mu m^2$. The tip is a Pt wire manually cut, with diameter $\oslash = 125\,\mu m$.

4.5.1 Cleaning procedure

The microfabrication processing leaves residues of PMMA, acetone and isopropanol on the sample surface. An atomically clean surface is essential for STM measurements, therefore a reliable cleaning procedure is required.

The standard cleaning procedure that makes use of temperature annealing in the UHV chamber via a button heater proves not to be sufficient to clean the samples.

Temperature annealing for 6 h at 280°C caused a significant degassing of the sample which resulted in a pressure raise of about 2 orders of magnitude in the UHV chamber. After this treatment it was possible to approach with the tip on the sample and to scan (Fig. 4.8(B)). However, the amplitude of the noise in the tunneling current signal was three orders of magnitude higher than usual and attempts to zoom in, in order to resolve small structures, were unsuccessful.

The current annealing method [13] resulted instead in a clean surface on which atomic resolution could be achieved. One hour of current annealing with I=1 mA and corresponding J=1.0·10^6 A/cm^2 (the width of the graphene layer is 300 μm and we assume that the thickness is t=0.345 nm) did not improve the surface quality, and the noise in the tunneling current signal had the same amplitude as before the current flow. One additional hour of current annealing with I=3 mA and corresponding J=3.0·10^6 A/cm^2 resulted instead in a clean surface, on which atomic resolution was achievable (Fig. 4.8(C)). Additionally, after the last cleaning treatment, the amplitude of the noise in the tunneling current signal lowered to usual values.

A surface roughness analysis in the STM images confirms the success of the cleaning process. The average roughness is defined as

$$R_a = \frac{1}{N}\sum_{j=1}^{N}|r_j|$$

where r_j is the deviation from the mean height value. Before lithography (Fig. 4.8(A)) the graphene sheet has an average roughness $R_a \sim 0.16$ nm. After lithography and temperature annealing (Fig.4.8(B)) the average roughness is $R_a \sim 0.30$ nm, and after the current annealing (Fig. 4.8(C)) is $R_a \sim 0.17$ nm.

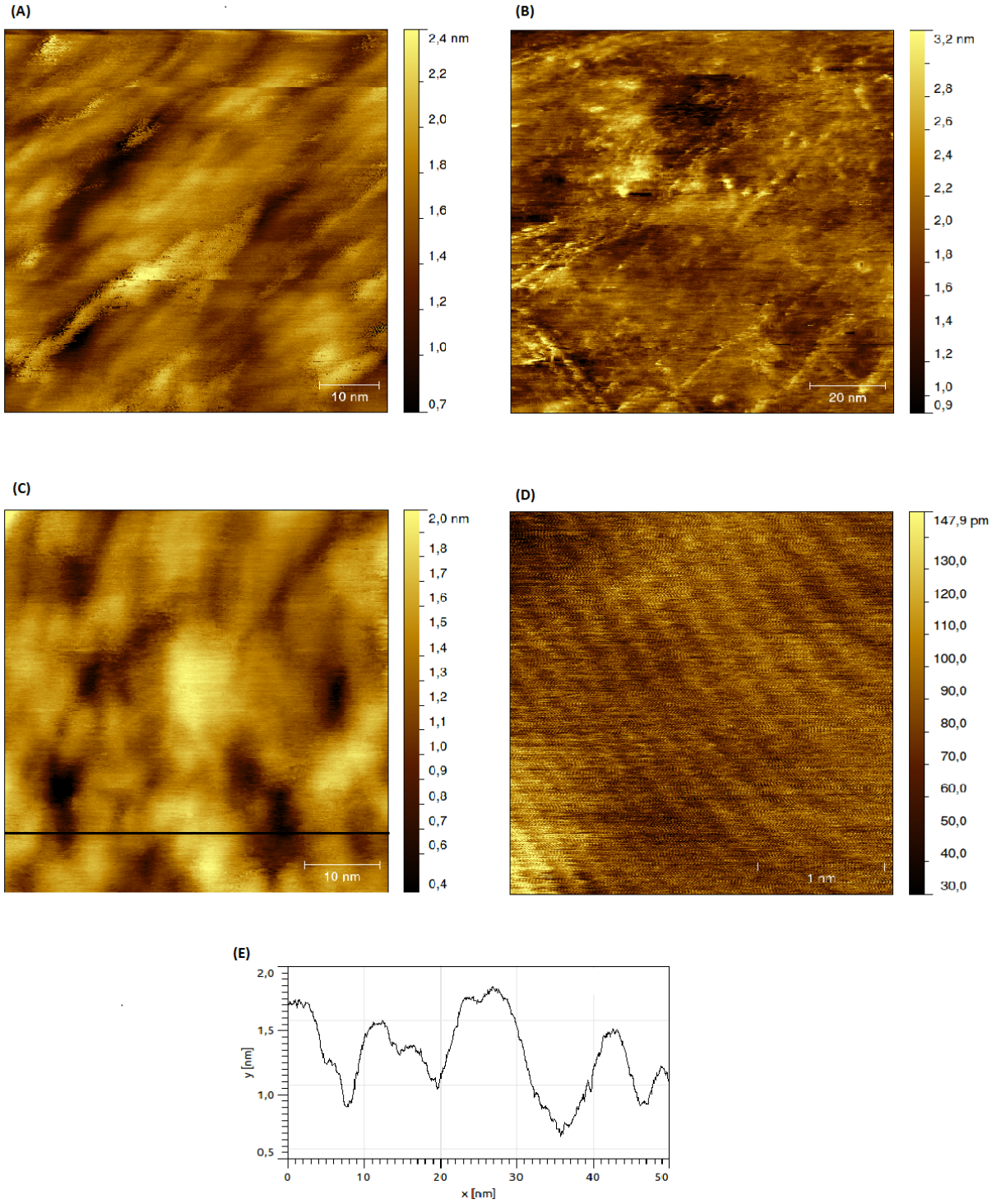

Figure 4.8: **(A)** STM image of the graphene sample before lithography (1 V, 1.0 nA). **(B)** STM image of the microfabricated sample after 6 h of temperature annealing at 280°C (0.5 V, 1.0 nA). **(C)** STM image of the microfabricated sample at the end of the cleaning procedure (0.5 V, 1.0 nA). **(D)** Zoom in on the image (C). The atomic lattice can be observed (0.5 V, 1.0 nA). **(E)** Line scan obtained along the black line in image (C).

Chapter 5

Molecules on HOPG

The second goal of this thesis is to find molecules that bind on graphene at room temperature, forming small clusters. In the preliminary studies, deposition of molecules is done on HOPG (Highly Oriented Pyrolitic Graphite), since the measurements are performed while the graphene samples are still under fabrication and HOPG has a surface structure similar to that of graphene. The interaction of three different kinds of molecules with HOPG are investigated.

In this section the possible interactions between molecules and surfaces from a theoretical point of view will be presented, as well as the principles of scanning tunneling spectroscopy and the results that we obtained from molecules deposition on HOPG.

5.1 Physisorption and chemisorption

The adhesion of atoms or molecules of a gas to a solid surface is called adsorption. It happens due to a surface effect: since the atoms on the surface are not fully surrounded by other atoms, as they are in the bulk phase, they can have free dangling bonds that can attract adsorbates.

The adsorption of an atom or molecule on a solid surface involves the same basic forces that are known from the quantum-mechanical theory of chemical bonding. In this case, however, one of the partners is a macroscopic medium with an infinite number of electrons, whose 2D surface is exposed to the other microscopic bonding partner.

The nature of the bonding that is involved in adsorption is addressed by the terms *physisorption* (physical adsorption) and *chemisorption* (chemical adsorption).

In physisorption the electronic structure of molecules or atoms is hardly perturbed upon adsorption. The attraction is due to van-der-Waals forces generated by mutually induced dipole moments.

In chemisorption the bonding mechanism resembles the formation of covalent or ionic bonds in molecular physics. The electronic structure of the bonding partners is strongly perturbed, new hybrid orbitals are formed, and there may be charge transfer from one partner to the other.

5.2 Spectroscopy on molecules

Together with topographic images, STM provides another technique to study the electronic structure of surfaces, i.e. tunneling spectroscopy, which measures the local density of states as a function of the electron energy. The technique consists of placing the STM tip over a specific location on the surface, with the feedback loop switched off, and measuring the tunneling current while the bias voltage (and thus the energy of electrons) is varied. Typical results of spectroscopy measurements are I-V curves and their derivative dI/dV-V.

If the sample investigated is just a metallic sample, I-V curves are expected to be linear, since there is no gap between the conduction band and the valence band, and the variation in density of states is very small. However, if a molecule, or a layer of molecules, is present above the substrate, the I-V curves can change their behaviour, depending on the electronic properties of the molecules. Molecules have discrete energy levels, therefore their conductance changes when the bias voltage is changed (Fig. 5.1(A)). If the bias voltage is low, it could happen that no energy levels of the molecules are accessible to the tunneling electrons, therefore the molecules show insulating behaviour and the only tunneling current measured is the one that goes straight from the sample to the tip. When a higher bias voltage is applied, however, some energy levels of the molecules become accessible to tunneling electrons and the molecules acquire conducting behaviour. The tunneling current increases since an additional tunneling channel is open. Therefore typical I-V curves for molecules show an almost flat trend of I for small V, with a steep increase of current above a certain value of V (Fig. 5.1(B)).

Comparison between I-V curves acquired on the bare substrate and above a bright feature can help to characterize the nature of the bright feature.

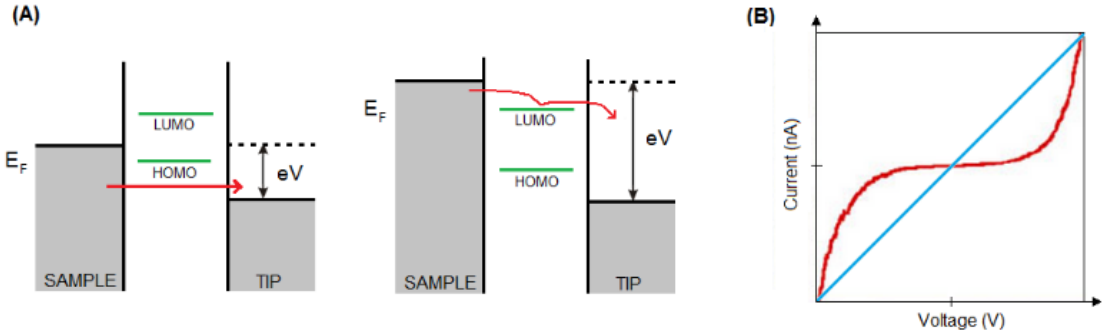

Figure 5.1: **(A)** Electron tunneling mechanism when a molecule with discrete energy level is deposited on the sample surface. The conductive properties of the system change if the bias voltage is changed. **(B)** Comparison between ideal I-V curves acquired on metal (blue) and on molecules (red).

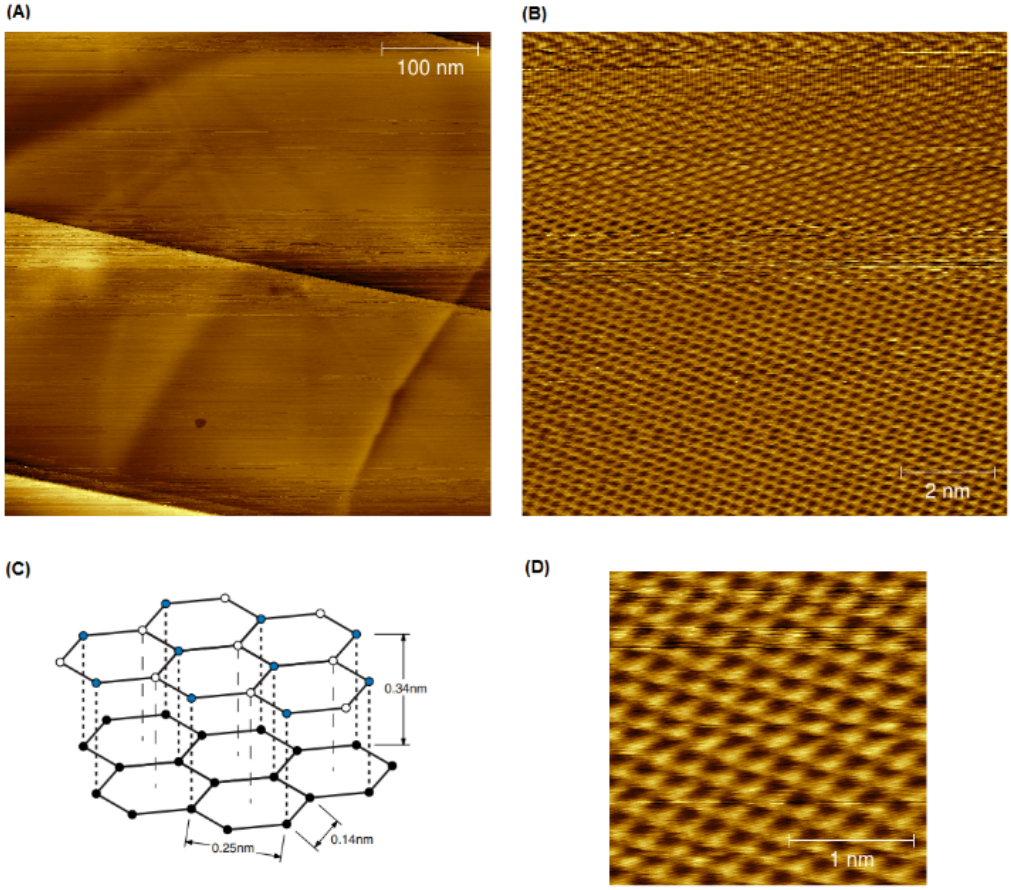

Figure 5.2: **(A)** Large area STM image of HOPG showing 3 step edges (0.6 V, 1 nA) **(B)** STM atomic resolution image of HOPG in which the hexagonal lattice is revealed (0.6 V, 1 nA). **(C)** Structure of the lattice of HOPG, in which the A-type and the B-type atoms are shown respectively in blue and white. **(D)** STM atomic resolution image of HOPG in which the triangular lattice is revealed (0.6 V, 1 nA). The bright spots correspond to A-type atoms, which lie on top of an A-type atom in the adiacent lower layer.

5.3 HOPG

Natural graphite exhibits quite imperfect structure due to plenty of defects and inclusions. Pyrolytic graphite is a graphite material with a high degree of preferred crystallographic orientation of the axes perpendicular to the surface of the substrate. It is obtained by graphitization heat treatment of pyrolytic carbon or by chemical vapor deposition at high temperatures. HOPG is a highly-ordered form of high-purity pyrolytic graphite. It is commonly used in scanning probe microscopy as a substrate, or as a calibration standard at atomic levels of resolution.

HOPG belongs to lamellar materials because its crystal structure is characterized by an arrangement of carbon atoms in stacked parallel layers: graphite structure can be described as an alternate succession of graphene planes. The lattice of graphene consists of two equivalent interpenetrating triangular carbon sublattices A and B (Section 2.4.1). In bulk HOPG, A- and B-sites carbon atoms become

inequivalent: every A-type atom in the upper (surface) layer is located directly above an A-type atom in the adjacent lower layer, whereas B-type atoms do not lie directly below or above an atom in the other layer, but sit over a void (Fig. 5.2(C)).

Thus in each layer the atoms form a grid of correct hexagons with distances between atoms equal 0.14 nm. The distance between layers is equal 0.34 nm.

In an atomic resolution STM image of HOPG, there are two possible images: depending on the conditions of the tip, the hexagonal lattice or the triangular structure can be revealed. Under ideal conditions, STM images of HOPG surface reveal a lattice of dark spots with a lattice parameter of 0.25 nm. The six carbon atoms surrounding each spot give a bright signal, which leads to a true honeycomb atomic pattern. The center to center atomic distance is 0.14 nm (Fig. 5.2(B)). The atomic pattern normally observed in most STM images of graphite under usual conditions shows the triangular lattice: bright spots originate only from the A-type carbon atoms. Each apparent atom is surrounded by six nearest neighbors. The distance between any two of these atoms is 0.25 nm (Fig. 5.2(D)).

5.4 Evaporation of molecules on HOPG

Molecules are evaporated in the UHV preparation chamber of the STM, by means of a Knudsen cell which is separated from the chamber by a gate valve that is open only during evaporation.

Before each evaporation, the HOPG sample is cleaved with Scotch tape, annealed in UHV at 120°C for 45 min and scanned on large areas as well as on small areas until atomic resolution is achieved, in order to confirm that the surface is clean. Typical STM images of HOPG are shown in Fig. 5.2.

The molecules, which are in a powder state, are loaded in a crucible where the temperature can be precisely controlled. The degassing of the molecular source is important since we use commercial products, which purity is generally of the order of 95-98%. Remaining materials are usually solvents or byproducts in the processing cycle; they appear as additional adsorbates and are therefore considered as dirt. Before each evaporation the crucible is heated up for several hours at a temperature slightly lower than the molecules' sublimation temperature, in order to eliminate dirt and undesired contaminants.

The evaporation process is controlled by monitoring the temperature and the pressure. Moreover, a mass spectrometer is mounted onto the STM preparation chamber during the evaporation procedure and mass spectra are recorded. After the degassing of the K-cell for several hours, the gate valve that connects the evaporator with the chamber is open, and mass spectra and pressure are monitored while the temperature is gradually increased towards the molecules' sublimation temperature. When the sublimation temperature is reached, the sample is put straight in front of the evaporator for the desidered amount of time.

The interactions of three different molecules with the HOPG surface are investigated (Fig. 5.3): metal-free phthalocyanine (H_2Pc), tetraphenylphosphonium chloride (TPPC) and oligo(phenylene-ethynylene)s (OPEs).

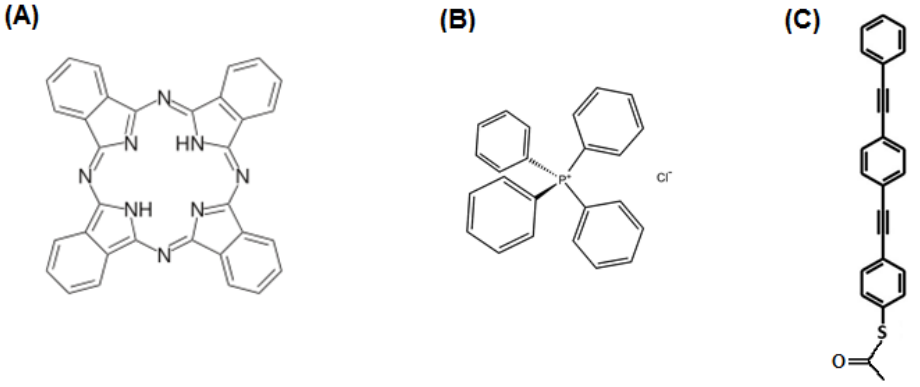

Figure 5.3: **(A)** Metal-free phthalocyanine. **(B)** Tetraphenylphosphonium chloride. **(C)** Oligo(phenylene-ethynylene)3 with a sulfur-acetyl group.

Phthalocyanine on HOPG

Metal-free phthalocyanine, or H_2Pc (Fig. 5.3(A)), are big flat molecules of an intense blue color, that are widely used as dyes. They were purchased in powder state from Sigma-Aldrich (purity 98%), and they have a sublimation temperature above 300°C. These molecules were evaporated both on HOPG and on graphene samples. The exposure time of the samples in front of the evaporator was about 30-60 sec (from previous experiments of evaporation of the same molecules on a gold sample in our setup, full coverage of the surface with molecules was obtained after 30 sec of exposure). After the deposition no molecules were observed on the STM images. STM studies of phthalocyanine deposited on HOPG are reported in literature [35, 36, 37], however measurements are generally done at low temperatures. Therefore we concluded that at the room temperature these molecules weakly interact with the surface of HOPG, and they are probably too mobile to be detected.

Tetraphenylphosphonium chloride on HOPG

Tetraphenylphosphonium chloride, or TPPC (Fig. 5.3(B)), is a salt available in the form of a white powder (purchased from Sigma-Aldrich, purity 98%). The sublimation temperature is ∼270°C. We did two evaporations of these molecules on HOPG, both with a 40 sec exposure time. After the first evaporation, bright lines on most of the step edges of HOPG were observed. A long "chain" that crosses a large area of the sample showing a regular structure is also observed, however its origin is not clear. After the cleaving of the sample and second evaporation, both features (bright stripes and chain structure) were observed again. Atomic or molecular resolution of these structures in not achievable, and spectroscopy measurements do not clearly reveal the typical I-V curves expected for molecules. STM studies of TPPC on HOPG are not reported yet, therefore the chain structures should be investigated further. Chainlike arrangements of clusters of a different type of molecules are already observed after deposition on HOPG by solution [38]. The type of interaction that TPPC molecules have with the surface, even if interesting,

is not significant for this thesis, therefore is not investigated further.

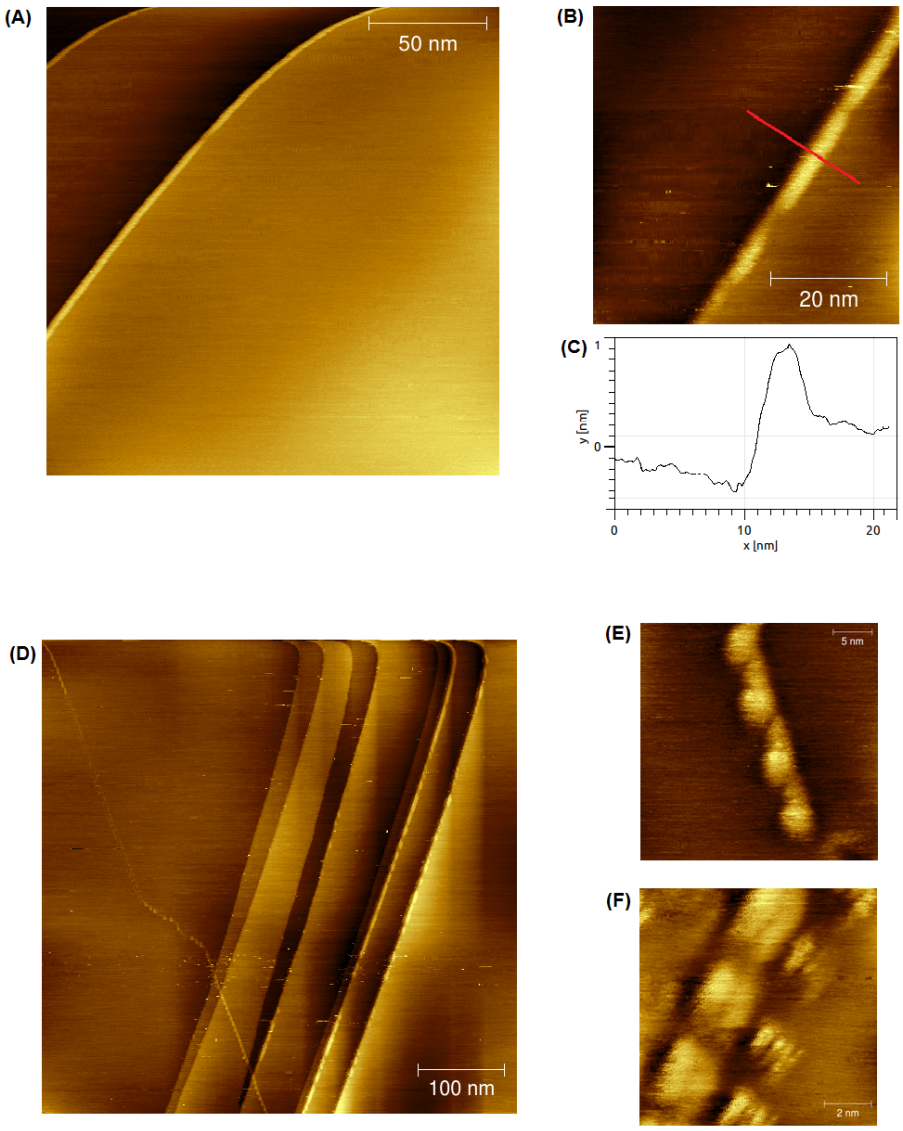

Figure 5.4: STM images of HOPG after TPPC evaporation. **(A)**, **(B)** Bright features on the step edges (0.8 V, 1.0 nA). **(C)** Line scan obtained along the red line in (B). The bright features are ∼500 pm in height. **(D)** Chain structure that cross the surface and bright features on step edges (1.0 V, 1.0 nA). **(E)** Zoom in of the chain structure in (D) (1.0 V, 1.0 nA). **(F)** Zoom in of the chain structure after the second evaporation (0.6 V, 1.0 nA).

Oligo(phenylene-ethynylene)s on HOPG

Oligo(phenylene-ethynylene)s are conjugated molecules well known in molecular electronics for their switching properties. We use OPE3-monoS-Ac (Fig. 5.3(C)), which present three benzene rings and a sulfur-acetyl group at one end; they are home-synthesized in form of a white-yellow powder. Their sublimation temperature is ∼120°C.

STM studies of these molecules on HOPG are reported in literature [39], with the formation of ordered self-assembled monolayers with the molecules laying horizontally on the surface. The deposition on HOPG is in general done from solution and not by evaporation. Studies of OPE3 deposited by evaporation are reported in literature only on gold [40], where the interactions with the gold substrate is different due to the thiol group that binds to the gold surface. In this case the molecules form a self-assembled monolayer with the molecules that stand vertically on the surface.

In our experiment the exposure time of the sample in front of the evaporator was 120 sec. After the evaporation we found clusters of molecules of 5-10 nm, distributed in different places all over the surface investigated (Fig. 5.6). In the areas where the clusters were not present, atomic resolution of the HOPG lattice was achieved.

On the contrary, it is not possible to resolve the molecular or submolecular structure of the clusters. The different behaviour of the interactions between OPE3 and HOPG from the one reported in literature could be due to the temperature of the substrate during the deposition or to the deposition time. However, the formation of small clusters is more suitable for the purpose of our project than the formation of a self-assembled monolayer.

Spectroscopy measurements (I-V curves) were done on this sample, on the clusters of molecules as well as on the HOPG substrate, showing the expected different behaviour of molecules and conductive substrates (Fig. 5.5).

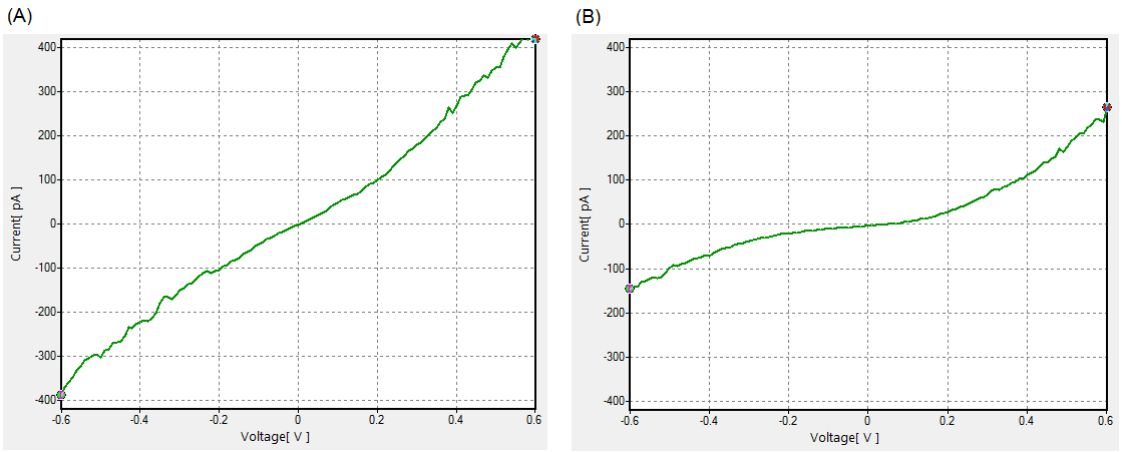

Figure 5.5: I-V curves obtained from the average of 20 I-V curves consecutively acquired in the same location. In (A) the tip is placed on the conductive HOPG substrate, and the I-V shows the typical linear behaviour. In (B) the tip is placed upon a cluster of molecules, and a departure from the linear behaviuor is observable.

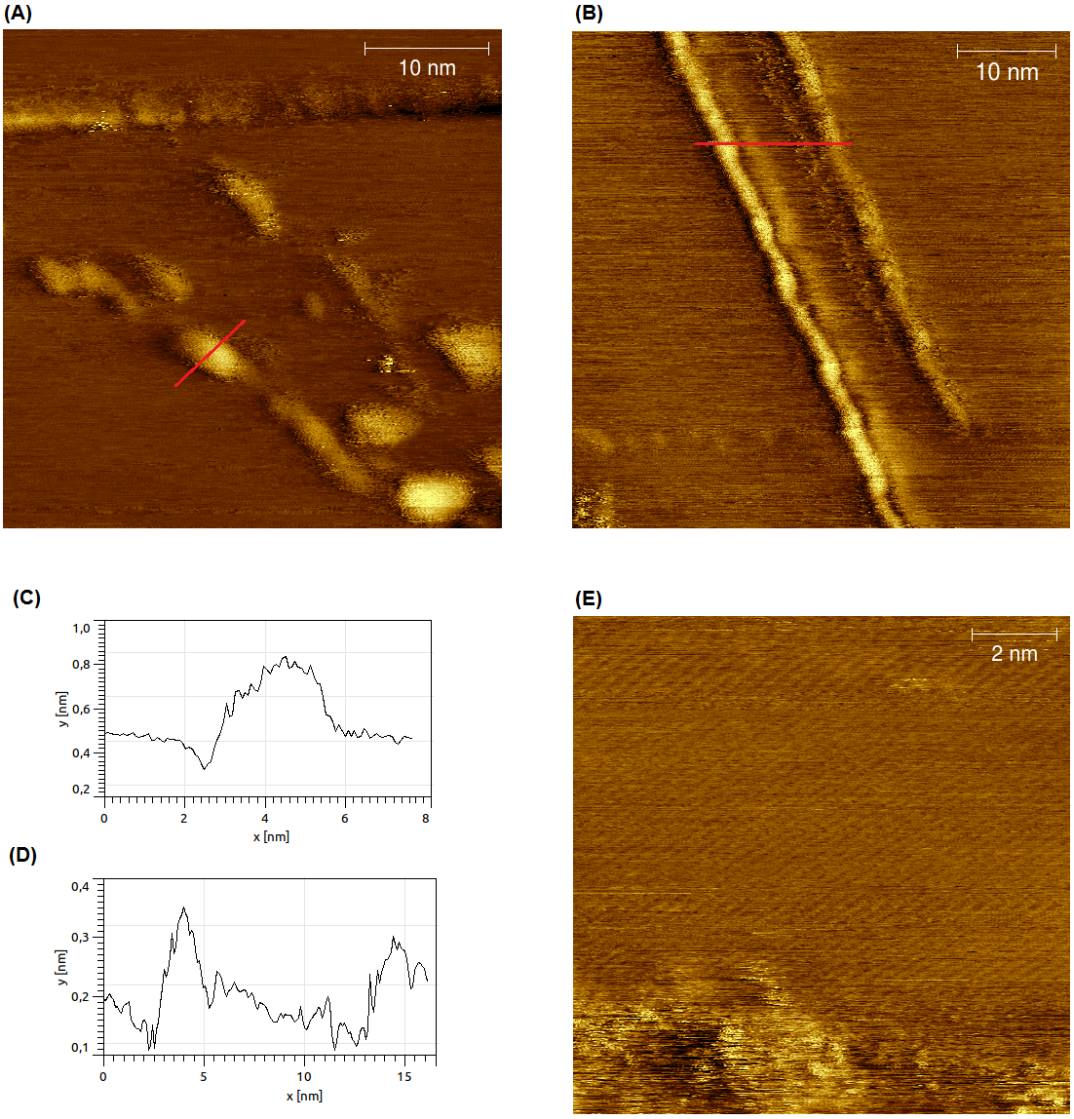

Figure 5.6: **(A)** STM image of OPE3 deposited on HOPG. In the upper part a step edge decorated with molecules can be observed, in the lower part molecules are forming small clusters (0.8 V, 0.8 nA). **(B)** Other linear structures formed by molecules in a different location on the surface (0.8 V, 0.8 nA). **(C)** Line scan obtained along the red line in (A). The height of the clusters is ∼400 pm. **(D)** Line scan obtained along the red line in (B). **(E)** Atomic resolution on HOPG, as well as clusters of molecules (in the lower part) are observable (0.8 V, 0.8 nA).

Chapter 6

Conclusions and Outlooks

In the findings reported in this project, two main topics were investigated: the procedures for microfabricating graphene samples, and the STM studies of different molecules deposited on HOPG. The final goal of isolating single molecules on graphene and observing how they can be moved by the current has not been reached yet.

By using the CVD-grown graphene provided by Graphene Supermarket, a good procedure for patterning the graphene samples was developed. The necessity of reaching high current densities requires small graphene samples, however, at the same time, the samples need to be big enough to allow a safe approach of the STM tip on the conducting graphene surface. As a tip, we used a Pt wire with diameter 125 μm, that allowed us to land safely on a $300\times300\mu m^2$ graphene surface, on which current densities up to $10^6 A/cm^2$ were easily reached without damaging the sample.

Using STM to study samples made with microfabrication techniques constituted a challenge for the cleaning procedure. Microfabrication leaves many residues on the samples, while STM measurements require clean samples. A reliable and repeatable cleaning procedure that exploits current-cleaning and the phenomenon of electromigration was developed and successfully used.

Graphene provided from the Graphene Supermarket proved to be sufficiently good for our initial experiment. However, the samples present some cracks and wrinkles on the surface. Due to the low quality of the graphene, some of the samples produced with lithography proved to be unusable, since they presented too many damaged zones. Therefore, in order to safely proceed with the project, other sources of better quality graphene need to be investigated.

The other source of graphene that we investigated, i.e. graphene synthesized by mechanical exfoliation, produced graphene flakes that were too small in order to allow a safe approach of the STM tip in our current experimental setup. However, solutions could in principle be reached. The simplest solution would be to fabricate the gold contacts in a way that they surround the graphene flake, allowing a safer approach on gold. After the approach, the graphene could be reached by following additional structures that could be patterned on gold in the microfabrication step.

Alternatively other graphene sources could be investigated, such as CVD graphene of better quality, or graphene grown on SiC.

From the deposition of molecules on HOPG we obtained the following results. Metal-free phthalocyanines did not bond well to the surface of HOPG and we did not detect them after the evaporation. The deposition of tetraphenylphosphonium chloride resulted in the formation of bright features on the step edges, as well as the chain-like structures. These features could not be atomically resolved, and spectroscopy measurements did not show significant differences between the HOPG and the structures. The origin of these structures is thus not completely clear, and it would be interesting to investigate them. In any case, these structures are not what this project is aiming for, therefore we did not investigate them further. The deposition of OPE3 molecules resulted in the formation of small clusters all over the surface. The clusters could not be atomically resolved, however spectroscopy measurements confirmed the conductance difference between the conductive substrate and the clusters. These molecules provided the best results for the aim of the project during our investigations, and they will be used in the next step of the experiment.

In these preliminary studies and results, we found a reliable procedure to fabricate and clean the samples, and we deposited and observed molecules that formed small clusters on HOPG.

The next step of the project will be the deposition of the OPE3 molecules on the graphene sample with the microfabricated contacts, and the subsequent investigation of the current-induced motion. Single molecules can be obtained either by manipulation with the STM tip or by exploiting low temperatures. Electromigration of single molecules on graphene then could be investigated. In order to reveal the non-conservative component of the driving force, as it is suggested in the paper of Dundas [2], it is necessary to study the current-induced motion of single atoms, therefore low temperatures will be necessary, and the experiment will move on the low-temperatures STM.

During this preliminary studies, the bases for the study of electromigration of molecules on graphene were successfully prepared, and the project is now ready to proceed in the investigation of current-induced forces.

Appendix A

Born-Oppenheimer and Ehrenfest approximation

In solid state physics, a monoatomic solid can be represented by N nuclei with mass M and electric charge Ze, and $n = ZN$ electrons with mass m. The time-independent Schrödinger equation of the system is

$$H\psi(\vec{r}_i, \vec{R}_I) = E\psi(\vec{r}_i, \vec{R}_I)$$

where ψ is the wavefunction of the whole system, $\vec{r}_i$ are electron positions, $\vec{R}_I$ are nuclei positions and H is the crystal Hamiltonian, which has an electronic part, a nuclear part and a nuclei-electrons interaction term:

$$H = -\sum_{I=1}^{N} \frac{\hbar^2}{2M}\nabla_I^2 - \sum_{i=1}^{n} \frac{\hbar^2}{2m}\nabla_i^2 + \frac{1}{2}\sum_{i\neq j} \frac{e^2}{|\vec{r}_i - \vec{r}_j|} + \frac{1}{2}\sum_{I\neq J} \frac{(Ze)^2}{|\vec{R}_I - \vec{R}_J|} - \sum_{i,J} \frac{Ze^2}{|\vec{r}_i - \vec{R}_J|}$$

It can be shortly expressed as $H = T_N + T_e + V_{ee} + V_{NN} + V_{eN}$. An exact solution of the Schrödinger equation is not possible and approximations must be made.

Born-Oppenheimer approximation

The Born-Oppenheimer approximation, or adiabatic approximation (Born, Oppenheimer, 1927), relies on the fact that there is a strong separation of time scales between the electronic and nuclear motion, since the electrons are lighter than the nuclei by three orders of magnitude.

In this approximation, the degrees of freedom of the electrons and the ions can be uncoupled: for each position of the nuclei, the electrons can be relaxed to the ground state, and the energy for that configuration can be calculated, without considering the interactions between moving electrons and ions. The wavefunction can therefore be split into two parts, a nuclear wavefunction and an electronic wavefunction, which depends parametrically on the nuclear positions:

$$\psi(\vec{r}, \vec{R}) = \phi_N(\vec{R})\chi_e(\vec{r}, \vec{R})$$

Another consequence of the mass difference between electrons and nuclei is that the nuclear components of the wave function are spatially more localized than the electronic components of the wave function. It follows that the nuclear wave function rises more steeply than the electronic one, which means that $\nabla_I \phi_N \gg \nabla_I \chi_e$. Therefore, if we apply the kinetic operators to the wavefunction we can neglect some of the terms, obtaining the following approximation:

$$T_e \phi_N \chi_e = -\sum_{i=1}^{n} \frac{\hbar^2}{2m} \nabla_i^2 \phi_N \chi_e = \phi_N T_e \chi_e$$

$$T_N \phi_N \chi_e = -\sum_{I=1}^{N} \frac{\hbar^2}{2M} [\phi_N \nabla_I^2 \chi_e + \chi_e \nabla_I^2 \phi_N + 2(\nabla_I \chi_e)(\nabla_I \phi_N)] \simeq \chi_e T_N \phi_N$$

The Schrödinger equation can be rewritten dividing all the terms by $\phi_N \chi_e$:

$$\frac{(T_e + V_{ee} + V_{eN})\chi_e}{\chi_e} = E - \frac{(T_N + V_{NN})\phi_N}{\phi_N} = \varepsilon(\vec{R})$$

where we noticed that the left side can only be a function of $\vec{R}$ alone.

Therefore, we obtain an electronic eigenvalue equation for the electronic Hamiltonian $H_e = T_e + V_{ee} + V_{eN}$, with a set of eigenfunctions and eigenvalues that depend parametrically on the nuclear positions $\vec{R}$:

$$H_e \chi_e(\vec{r}, \vec{R}) = \varepsilon(\vec{R}) \chi_e(\vec{r}, \vec{R})$$

For each electronic eigenvalue $\varepsilon_n(\vec{R})$, the nuclear dynamics is described by a time-dependent Schrödinger equation for the time-dependent nuclear wave function $\phi(\vec{R}, t)$:

$$[T_N + V_{NN} + \varepsilon(\vec{R})]\phi(\vec{R}, t) = i\hbar \frac{\partial}{\partial t} \phi(\vec{R}, t)$$

Nuclei can also be considered as a classical system, since their wavefunctions are spatially more localized than the electronic ones: in that case the back action of the electronic quantum mechanical system on the nuclear motion is given by the force $\vec{F}_I$ exerted by the electrons on the ion that sits at the $\vec{R}_I$ position:

$$\vec{F}_I = -\frac{\partial \varepsilon}{\partial \vec{R}_I} = M \frac{d^2 \vec{R}_I}{dt^2}$$

The Hellmann-Feynman theorem (Hellmann 1937, Feynman 1939), valid for closed system in the equilibrium state, is usually applied to find forces exerted by electrons on atoms. It shows that the force on ions can be derived as the expectation value of the derivative of the electronic Hamiltonian with respect to ionic positions. Given that:

$$\varepsilon(\vec{R}) = \langle \chi_e | H_e(\vec{R}) | \chi_e \rangle$$

from the Hellmann-Feynman theorem, the force on ions can be calculated as:

$$\vec{F}_I = -\frac{\partial \varepsilon(\vec{R})}{\partial \vec{R}_I} = -\langle \chi_e | \frac{\partial H_e}{\partial \vec{R}_I} | \chi_e \rangle$$

Due to the Hellmann-Feynman theorem, the force, as well as the energy, can be calculated for a given atomic configuration without recalculating the electronic states. This make force calculations simpler and more manageable in terms of time.

Ehrenfest approximation

The Born-Oppenheimer approximation can fail when the ions move sufficiently fast that the electronic subsystem will not have time to minimize its free energy before the ions undergo substantial further displacement.

This mechanism for departures from the Born-Oppenheimer approximation is taken into account by the Ehrenfest approximation, which is a simple approach to include non-adiabatic interactions between electrons and ions in time-dependent quantum-mechanical simulations [44]. In Ehrenfest dynamics, the ions are treated as classical particles moving in a mean-field generated by the electrons. In turn, the electrons are modelled as fully quantum mechanical particles evolving in a time-dependent potential generated by the ions.

Therefore the ions, as classical particles, are localized in space and their dynamics are completely characterized by their positions as a function of time.

The Ehrenfest equations, which are exact, allow us to map the quantum expectation values of ionic positions $\vec{R}$, momenta $\vec{P}$ and forces $\vec{F}$ onto the corresponding classical quantities, yielding the following equations of motion:

$$\frac{d\vec{R}}{dt} = \frac{\vec{P}}{M}\,, \qquad \frac{d\vec{P}}{dt} = \vec{F}\,, \qquad \vec{F} = -\mathrm{Tr}\left\{\hat{\rho}\frac{\partial \hat{H}}{\partial \vec{R}}\right\}$$

Here $\hat{\rho}$ is the full density matrix for the system of electrons and ions, $\hat{H}$ is the full Hamiltonian, $\vec{R} = \mathrm{Tr}\{\hat{\rho}\hat{R}\}$ and $\vec{P} = \mathrm{Tr}\{\hat{\rho}\hat{P}\}$, where $\hat{R}$ and $\hat{P}$ are the operators for ionic coordinates and conjugate momenta.

The goal is to find $\hat{\rho}$, however in general this is difficult, and instead expectation values that involve the density matrix are usually calculated. The equation of motion for these expectation values are numerically easier to work with, compared to the full density matrix.

In the Ehrenfest approximation, instead of considering the density matrix for the whole system of electrons and ions, the only electronic density matrix $\hat{\rho}_e$ is retained: in this way any explicit correlation between electrons and ions is eliminated. Therefore the equations of motion become:

$$\vec{F} = -\mathrm{Tr}\left\{\hat{\rho}_e \frac{\partial \hat{H}_e}{\partial \vec{R}}\right\}, \qquad i\hbar\frac{d\hat{\rho}_e}{dt} = [\hat{H}_e(\vec{R}), \hat{\rho}_e]\,, \qquad \frac{d\vec{P}}{dt} = \vec{F} - \vec{\nabla} V_{NN}(\vec{R})$$

where in the momentum dynamics the ion-ion interaction is also taken into account.

The equations just derived correspond to the Ehrenfest approximation, which is valid only for sufficiently massive or energetic ions, over restricted timescales. Due to the absence of explicit correlations between electrons and ions, Joule heating does not arise from these calculations. In order to take into account Joule heating, approximations to higher orders have to be investigated [45]. However, the

Ehrenfest approximation can already be exploited if Joule heating does not play an important role in the matters of interest, and it provides a useful intuitive way to understand ionic motion.

Bibliography

[1] R.S. Sorbello, *Theory of Electromigration*, Acad. Press (1998), pp. 159-231

[2] D. Dundas et al., Current-driven atomic waterwheels, Nature Nanotechnol., 4, 99-102 (2009)

[3] K.N. Tu, Recent advances on electromigration in very-large-scale-integration of interconnects, J. Appl. Phys. 94, No. 9 (2003)

[4] P. S. Ho, T. Kwok, Electromigration in metals, Rep. Prog. Phys. 52 301 (1989)

[5] R.S. Sorbello, C.S. Chu, Electronic conductivity and electromigration in metallic microstructures, Superlattices and Microstructures, Vol. 3, No.5 (1987)

[6] J. Park et al., Coulomb blockade and the Kondo effect in single-atom transistors, Nature 713, 722 (2002)

[7] H.B. Heersche et al., In situ imaging of electromigration-induced nanogap formation by transmission electron microscopy, Appl. Phys. Lett. 91, 072107 (2007)

[8] C. Tao et al., Visualizing the Electron Scattering Force in Nanostructures, Science 328, 736-740 (2010)

[9] J.-J. Mtois et al., Steady-state motion of silicon islands driven by a DC current, Surf. Science 420, 250-258 (1999)

[10] K. Svensson et al., Nanopipettes for Metal Transport, Phys. Rev. Lett. 93, 145901 (2004)

[11] B.C. Regan et al., Carbon nanotubes as nanoscale mass conveyors, Nature 428, 924-927 (2004)

[12] H. Yasunaga et al., Electromigration on semiconductor surfaces, Surf. Sci. Report 15, 205-280 (1992)

[13] J. Moser et al., Current-induced cleaning of graphene, Appl. Phys. Lett. 91, 163513 (2007)

[14] Todorov, Tight-binding simulation of current-carrying nanostructures, J. Phys. Condens. Matter 14, 30493084 (2002)

[15] R. Murali et al., Breakdown current density of graphene nanoribbons, Appl. Phys. Lett. 94, 243114 (2009)

[16] A.M. Goossens et al., Mechanical cleaning of graphene, Appl. Phys. Lett. 100, 073110 (2012)

[17] K. S. Novoselov, Two-dimensional gas of massless Dirac fermions in graphene, Nature 438, 197-200 (2005)

[18] A. K. Geim, K. S. Novoselov, The rise of graphene, Nature Materials 6, 183-191 (2007)

[19] A. H. Castro Neto et al., The electronic properties of graphene, Rev. Mod. Phys. 81, 109 (2009)

[20] D.R. Cooper et al., Experimental Review of Graphene, Condens. Matter Phys., 156 (2012)

[21] K. S. Novoselov et al., A roadmap for graphene, Nature 490, 192200 (2012)

[22] S. Reich et al., Tight-binding description of graphene, Phys. Rev. B 66, 035412 (2002)

[23] Z. H. Ni et al., Graphene Thickness Determination Using Reflection and Contrast Spectroscopy, Nano Letters 7 (9), 2758-2763 (2007)

[24] J. Hass et al., The growth and morphology of epitaxial multilayer graphene, J. Phys.: Condens. Matter 20, 323202 (2008)

[25] V. Emtsev et al., Towards wafer-size graphene layers by atmospheric pressure graphitization of silicon carbide, Nature Materials 8, 203 - 207 (2009)

[26] Y. Zhang et al., Review of Chemical Vapor Deposition of Graphene and Related Applications, Acc. Chem. Res. 46, 2329-2339 (2013)

[27] C.J. Chen, *Introduction to Scanning Tunneling Microsocopy*, Oxford University Press, (1993).

[28] P. Rai-Choudhury, *Handbook of Microlithography, Micromachining, and Microfabrication. Volume 1: Microlithography*, SPIE Press (1997)

[29] AllResist Datasheet, http://www.allresist.com/allresist_produktinfos_ar-p630-690_englisch.pdf

[30] https://graphene-supermarket.com/

[31] J. Banaszczyk, The Van der Pauw method for sheet resistance measurements, J. Appl. Polymer Science 117 (5), 2553-2558 (2010)

[32] Ishigami et al., Atomic Structure of Graphene on SiO_2, Nano Letters 7 (6), 1643-1648 (2007)

[33] V. Geringer et al., Intrinsic and extrinsic corrugation of monolayer graphene deposited on SiO2, Phys. Rev. Lett. 102, 076102 (2009)

[34] F. Atamny et al., On the STM imaging contrast of graphite : towards a true" atomic resolution, Phys. Chem. 1, 4113-4118 (1999)

[35] K. Nilson et al., Scanning tunneling microscopy study of metal-free phthalocyanine monolayer structures on graphite, J. Chem. Phys. 127, 114702 (2007)

[36] J. Ahlund et al., The adsorption of iron phthalocyanine on graphite: A scanning tunnelling microscopy study, Surface Science 601, 3661-3667 (2007)

[37] M. Scheffler et al., Structural study of monolayer cobalt phthalocyanine adsorbed on graphite, Surface Science 608, 5560 (2013)

[38] M.S. Alam et al., Spin-State Patterns in Surface-Grafted Beads of Iron(II) Complexes, Angew. Chem. Int. Ed. 49, 1159 1163 (2010)

[39] J. Gong et al., Molecular Organization of Alkoxy-Substituted Oligo(phenylene-ethynylene)s studied by Scanning Tunneling Microscopy, Langmuir 19 (24), 1012810131 (2003)

[40] N. Gergel-Hackett et al., Vapor Phase Deposition of a Monolayer of Organic Molecules for use in Molecular Electronic Devices, Journal of Vacuum Science and Technology 25 (1), 252 (2007)

[41] Z. Mu et al., Influence of Substituents on Two-Dimensional Ordering of Oligo(phenylene-ethynylene)s. A Scanning Tunneling Microscopy Study, Langmuir 20 (20), 8892 (2004)

[42] H. Ibach, H. Luth, *Solid-State Physics*, Springer (2009)

[43] H. Ibach, *Physics of Surfaces and Interfaces*, Springer (2006)

[44] T.N. Todorov, Time-dependent tight binding, J. Phys.: Condens. Matter 13, 10125-10148 (2001)

[45] A.P. Horsfield et al., Power dissipation in nanoscale conductors: classical, semi-classical and quantum dynamics, J. Phys.: Condens. Matter 16, 82518266 (2004)

[46] A. P. Horseld et al., Beyond Ehrenfest: correlated non-adiabatic molecular dynamics, J. Phys.: Condens. Matter 16, 8251-8266 (2004)